Motion-Compensated Steering: Enhanced Azimuthal Resolution for Polarimetric Rotating Phased Array Radar

David Schvartzman, *Member, IEEE*, Sebastián M. Torres, *Senior Member, IEEE*, and Tian-You Yu, *Member, IEEE*

***Abstract*— The rotating phased array radar (RPAR) is an architecture that could improve the capabilities of the current weather surveillance radar—1988 Doppler (WSR-88D) operational network and is likely to be more affordable than other candidate PAR architectures. However, continuous antenna rotation coupled with the need to perform coherent processing of multiple samples results in a degraded effective beamwidth (referred to as beam smearing) compared to architectures based on stationary antennas. The RPAR's beam agility can be exploited to reduce beam-smearing effects by electronically steering the beam on a pulse-to-pulse basis within the coherent processing interval. That is, the motion of the antenna can be compensated to maintain the beam pointed at the center of resolution volume being sampled. This motion-compensated steering (MCS) could reduce the effects of antenna motion and lead to a reduction in the effective beamwidth. The purpose of this article is to present and demonstrate the MCS technique for a dual-polarization RPAR system. In this article, we provide a formulation for the MCS technique, simulations to quantify its performance in mitigating beam-smearing effects, its impacts on the quality of dual-polarization radar-variable estimates, and a practical implementation on the National Severe Storms Laboratory's Advanced Technology Demonstrator (ATD) system. Experiments were carried out using two alternative concepts of operations (CONOPS) described in this article. Results show that a system designed with sufficient pointing accuracy can be operated as an RPAR using MCS, and the impact on radar-variable estimates is comparable to that obtained when operating the same system as a stationary PAR.**

***Index Terms*— Angular resolution, beamwidth, concept of operations, dual-polarization motion-compensated steering, phased array radar, weather radar.**

Manuscript received July 31, 2020; revised October 8, 2020, December 7, 2020, and January 7, 2021; accepted January 23, 2021. Funding was provided by NOAA/Office of Oceanic and Atmospheric Research under NOAA-University of Oklahoma Cooperative Agreement #NA16OAR4320115, U.S. Department of Commerce. *(Corresponding author: David Schvartzman.)*

David Schvartzman and Sebastián M. Torres are with the Cooperative Institute for Mesoscale Meteorological Studies, The University of Oklahoma, Norman, OK 73072 USA, also with the Advanced Radar Research Center, The University of Oklahoma, Norman, OK 73019 USA, and also with the Radar Research and Development Division, NOAA/OAR/National Severe Storms Laboratory, Norman, OK 73072 USA (e-mail: david.schvartzman@noaa.gov).

Tian-You Yu is with the Advanced Radar Research Center, School of Electrical and Computer Engineering, The University of Oklahoma, Norman, OK 73019 USA, and also with the School of Meteorology, The University of Oklahoma, Norman, OK 73069 USA.

Color versions of one or more figures in this article are available at https://doi.org/10.1109/TGRS.2021.3055033.

Digital Object Identifier 10.1109/TGRS.2021.3055033

I. Introduction

THE National Oceanic and Atmospheric Administration (NOAA) has started considering radar systems with advanced capabilities for the eventual replacement of the operational weather surveillance radar—1988 Doppler (WSR-88D). This network of approximately 160 radars surveys the atmosphere by mechanically rotating a parabolic-reflector antenna in azimuth and elevation following a prescribed volume coverage pattern (VCP). The WSR-88Ds have been operational for over 30 years and are still the primary observational instrument employed by National Weather Service (NWS) forecasters to support their mission. One of the most significant upgrades to the network in recent times involves the simultaneous transmission of electromagnetic waves with horizontal (H) and vertical (V) polarizations. In addition to estimating the spectral moments (reflectivity, Doppler velocity, and spectrum width), the signals received on the H and V polarization channels are used to compute the so-called polarimetric variables (differential reflectivity, differential phase, co-polar correlation coefficient), which provide information about the type and size of scatterers in the resolution volume [1], [2]. Nevertheless, the WSR-88Ds have exceeded their engineering design lifespan and are projected to reach the end of an operational lifetime by 2040 [3]. Although the WSR-88Ds still provide mission-critical data to support forecasters' in the issuing of severe weather warnings and forecasts, technological limitations may prevent this architecture to meet demanding functional requirements for future observational needs.

The NOAA Radar Functional Requirements document [4] specifies the functionality expected for a future weather surveillance radar system. The document's *Threshold Functional Requirements* are used to define the minimum expected performance of the future system, while its *Optimal Functional Requirements* define the desired system performance. One of the cost-driving threshold requirements specifies the angular resolution of the radiation patterns produced by the antenna system. The antenna pattern half-power beamwidth (HPBW), defined herein as the angular width in degrees within which the microwave radiation is greater than one-half of its peak intensity, is typically reduced by increasing the antenna aperture size. As specified by the threshold requirement, the system is expected to produce a radiation pattern that results in a narrow

HPBW of at most 1°. Due to continuous antenna rotation coupled with the need to perform coherent processing of multiple samples, the resulting *effective* antenna beamwidth (ϕ_e) is broader than the stationary inherent antenna beamwidth [5]. The effective beamwidth is controlled by the intrinsic physical beamwidth (ϕ_1), the antenna rotation rate (ω), the number of samples (M), and the pulse repetition time (T_s) [6]. As noted by Zrnić and Doviak [5], these parameters determine the normalized azimuthal sampling interval ($\Delta\phi$), which is the independent variable controlling the effective beamwidth. That is, the fractional beamwidth increase due to antenna motion and sampling, referred to as beam smearing, is a direct function of $\Delta\phi$. The value of $\Delta\phi$ for all cases illustrated in this article is 0.5, the same as that used in the WSR-88D super-resolution scans. Although no optimal requirement is specified in [4] for the effective beamwidth, researchers have demonstrated that the identification of velocity signatures from tornadoes is greatly improved when the azimuthal effective beamwidth of the radar is 1° or less [7], [8]. Therefore, it is desirable to design a cost-effective radar system that achieves this performance.

Unique capabilities offered by phased array radar (PAR) technology could support the required enhanced weather surveillance strategies that are envisioned to improve the timing and quality of weather radar products, making PAR technology an attractive candidate for the next generation of weather radars [9]. Ongoing research efforts that began in the early 2000s at the National Severe Storms Laboratory (NSSL) have been aimed at demonstrating unique PAR capabilities for weather surveillance [10]–[12]. The stationary four-faced planar PAR architecture has been the prime candidate system involving a multifunction phased array radar (MPAR) system [13] that would simultaneously support several missions [14]. This stationary radar architecture is not susceptible to beam broadening due to antenna motion and is capable of sampling the same resolution volume (defined by the HPBWs in azimuth and elevation, and the range resolution) for all transmitted pulses within the coherent processing interval (CPI) [15]. Nevertheless, it is well-known that the beamwidth of a stationary planar PAR system varies as a function of electronic steering angle, and it monotonically increases as the beam is steered away from broadside [16]. Brown and Wood [17] simulated the performance of this architecture for detecting tornado vortices. Their study found that the widest antenna beamwidth should be no more than ∼1° in order to provide NWS forecasters with "at least the same quality of data resolution that is currently available for making tornado and severe storm warnings." To ensure that the beamwidth on the edges of the scan sector (e.g., typically ±45° in azimuth and 0°–20° in elevation) is ∼1°, a broadside beamwidth of 0.758° is needed.

If PAR technology is to replace the currently operational parabolic-reflector-based WSR-88D, important decisions must be made regarding the architecture that will be needed to meet functional requirements. Although the stationary MPAR system is not susceptible to beam broadening effects, this concept has become a less feasible choice and current efforts

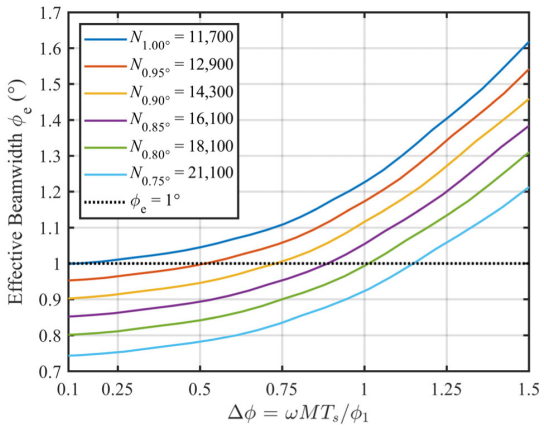

Fig. 1. Effective broadside beamwidth of planar RPAR systems of different sizes (N is the total number of antenna elements) as a function of the normalized azimuthal sampling, $\Delta\phi$.

are now centered on single-mission systems for weather surveillance [18]. A four-faced stationary PAR is likely capable of achieving the optimal requirements set forth by NOAA, but deploying and maintaining an operational network of these radars across the U.S. may be unaffordable. A more affordable alternative radar system is based on a single-faced rotating PAR (RPAR) architecture, which is capable of meeting all threshold requirements and of exceeding the capabilities of the current reflector-based network. Nevertheless, this architecture is susceptible to beam-smearing effects, and large aperture sizes may be required to achieve the desired effective beamwidth requirement. Fig. 1 illustrates the impact of $\Delta\phi$ on the effective broadside beamwidth of simulated planar RPAR systems of different sizes (where N_x is the total number of antenna elements for a stationary broadside HPBW of x°), with approximately circular apertures and a uniform grid of elements with half-wavelength spacing. The simulated transmit patterns have uniform tapering, and a Taylor tapering window is used on the elements of the simulated receive patterns to achieve the −40-dB two-way antenna peak sidelobe levels. For the receive patterns, linear Taylor tapers are applied along x and y, with five nearly constant-level sidelobes and maximum sidelobe levels of −55 dB. Notice that $\Delta\phi$ is determined by the pulse repetition time (T_s), the number of samples per CPI (M), ω, and ϕ_1. These results indicate that to achieve a ϕ_e of ∼1° for $\Delta\phi$ of up to 1 (typically known as "legacy" sampling in the WSR-88D), an aperture comprising ∼18,100 elements (and with a true azimuthal broadside beamwidth of ∼0.8°) is needed. It is desired to exploit advanced capabilities of the RPAR system to decrease the effective beamwidth, leading to reduced aperture sizes capable of meeting effective beamwidth requirements.

In this article, the RPAR's beam agility is exploited to reduce beam-smearing effects under a continuous azimuthal rotation regime. By electronically steering the beam on a pulse-to-pulse basis within the CPI, the motion of the antenna is compensated to maintain the beam pointed at the same earth-relative angular direction. This motion-compensated steering (MCS) could ideally remove the apparent motion of the

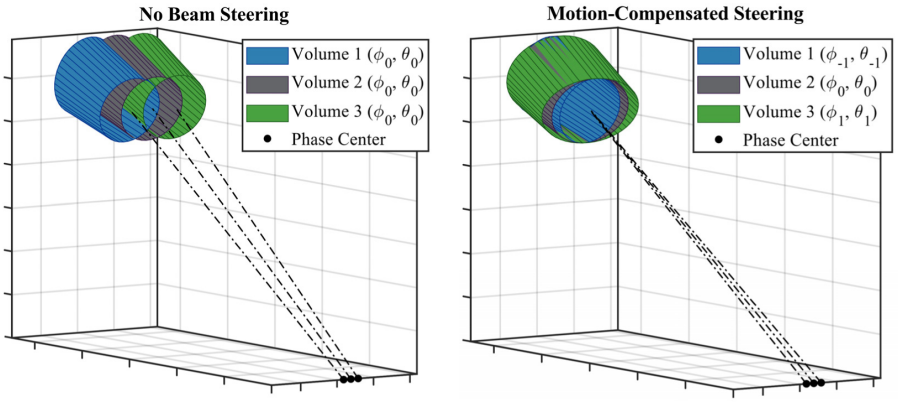

Fig. 2. Depiction of the MCS concept. (Left) Location of resolution volumes being sampled by the antenna without beam steering. (Right) Location of resolution volumes being sampled with MCS.

antenna and lead to a reduction in the effective beamwidth. In turn, mitigating the impact of beam smearing allows for smaller (and more affordable) antenna apertures that can meet angular resolution requirements. The focus of this article is to study the impact of MCS on weather-radar variables, to develop an RPAR simulation capable of quantifying the performance of MCS, and to implement a proof-of-concept MCS on a research RPAR system. The successful implementation and demonstration of this technique on dual-polarization weather RPAR could result in a considerable reduction in system cost for the eventual acquisition of an RPAR-based U.S. Weather Surveillance Radar.

The concept of MCS was initially developed for air surveillance and defense operations in the mid-1970s [19] and has since been widely used for synthetic aperture radar applications. Initial applications of this concept for meteorological observations were presented in 2002 by Law *et al.* [20] who compensated for platform motion for a shipborne, vertically pointed, L-band, passive PAR wind profiler system. Their experimental results showed that the electronically stabilized wind profiler measurements were in good agreement with profiles retrieved through simultaneous rawinsonde balloon launches. Bluestein *et al.* [21] demonstrated the use of a mobile single-polarization X-band RPAR system leveraging an existing military radar, the MWR-05XP, with "back scanning" capabilities to produce rapid volumetric observations of convective storms. This back-scanning technique was implemented through frequency hopping and allowed the beam to dwell at a nearly fixed azimuth angle to collect the required samples. Although they briefly described this motion-compensation concept, they did not provide sufficient evidence quantifying the tradeoffs associated with the technique nor to verify its performance.

The purpose of this article is to present and demonstrate the MCS technique for a weather-surveillance dual-polarization RPAR system. A theoretical formulation for the MCS technique is described in Section II along with concept of operations (CONOPS) for implementing MCS on an RPAR system. A simulation framework to quantify the performance of the MCS technique is presented in Section III. The performance of MCS for the mitigation of beam-smearing effects is quantified first, then, impacts on the quality of dual-polarization radar-variable estimates are investigated. Section IV describes the practical implementation of the MCS technique on NSSL's Advanced Technology Demonstrator (ATD) dual-polarization planar PAR system and presents results from data collection experiments. Important outcomes of this research are summarized in Section V.

II. MCS for Polarimetric Weather RPAR

To implement MCS, the RPAR's electronic beam agility is exercised on a pulse-to-pulse basis. That is, to maintain an earth-relative pointing angle (i.e., azimuth and elevation) for all transmitted pulses within a CPI, beams are continuously steered electronically to point at the center of the resolution volume that is being sampled. A resolution volume is defined herein as the volume of space circumscribed by the 6-dB contour of the two-way antenna pattern in azimuth and elevation and of the range weighting function in the range [6].

The concept of MCS is depicted in Fig. 2 in comparison to the conventional sampling of a mechanically scanning antenna (i.e., No Beam Steering). As the antenna rotates, phase centers for transmitted pulses are displaced[1] following an antenna rotation at $\omega = 21.5^\circ$ s^{-1} and for a typical CPI ($M = 15$, $T_s = 3$ ms). Herein, we define the antenna phase center as the location that most closely approximates the center of curvature of the radiating wavefront (i.e., the focal point), and from which the electromagnetic radiation spreads spherically outward [22]. The volumes depicted correspond to the first, middle, and last samples in the CPI. Notice that as the RPAR's beam is electronically steered away from the broadside, there are beamwidth variations in azimuth and elevation as a function of steering angle. Therefore, as opposed to the displaced uniform volumes sampled with the broadside scanning beam (Fig. 2, left), the concentric volumes sampled by MCS are not the same size (Fig. 2, right).

These aspects are studied in detail in Sections II-A–II-C. First, the MCS steering angles to maintain beam pointing in azimuth and elevation are derived for the antenna-relative coordinate system. Then, the variation in volume size as a function of steering angle is theoretically modeled to understand its

[1]This figure is presented to illustrate the MCS concept in contrast to the conventional scanning technique, thus, the phase center displacements are exaggerated to emphasize the difference.

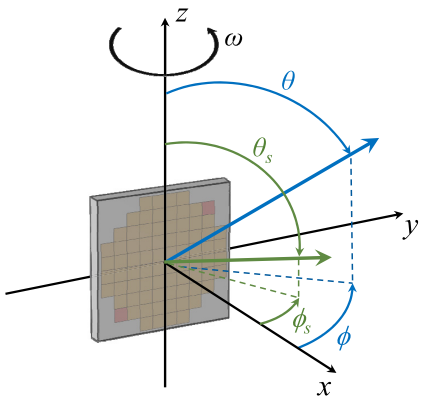

Fig. 3. Spherical coordinate system used to reference the RPAR scanning with MCS.

impact on the quality of radar-variable estimates. Lastly, two RPAR CONOPS using MCS are presented.

A. MCS Steering Angles

Assume that an RPAR is rotating about the z-axis at a rate of ω [° s^{-1}], in a spherical coordinate system with polar axis z vertical, and with x in the direction of North as indicated in Fig. 3. This coordinate system is tied to the earth, and therefore the *x-axis* is always directed to North. Note that the antenna lies on a plane that rotates about the z-axis and is orthogonal to the xy plane. This antenna geometry is convenient for modeling arrays designed to scan close to the horizon [23]. The desired scan pointing angle in the earth-relative spherical coordinate system is denoted as $(\phi_p,\ \theta_p)$. Note that $\phi_p = \phi_{az}$ and $\theta_p = 90° - \theta_{el}$, with ϕ_{az} and θ_{el} being the conventional earth-relative azimuth and elevation angles, respectively, and are the zenith and azimuth directions to the scatterers. Then, ϕ_N as a function of time is expressed as

$$\phi_N(t) = \phi_0 + \omega t \tag{1}$$

where ϕ_0 is the initial broadside position and t is time in seconds. For simplicity and without loss of generality, it is assumed that M is odd and that the radar is rotating in the clockwise direction. If the CPI is defined by M samples spaced by T_s, expression (1) can be discretized to produce the MCS steering angles as

$$\phi_{\mathrm{MCS}}(mT_s) = \phi_p - \phi_N = \left(\phi_p - \phi_0\right) + \omega\, T_s \left[\frac{(M-1)}{2} - m\right] \tag{2}$$

for $m \in \{0, 1, 2, \ldots, M-1\}$, and with $t = mT_s$. Note that ϕ_{MCS} is referenced to the earth's polar coordinate system. If the antenna is tilted by θ_T, with respect to the earth, the MCS pointing angles relative to the antenna coordinate system are given by (see Appendix A for details)

$$\begin{aligned}
&\phi^A_{\mathrm{MCS}}(mT_s) \\
&\quad = \arctan\left\{\frac{\sin\theta_p \sin[\phi_{MCS}(mT_s)]}{\sin\theta_p \cos[\phi_{\mathrm{MCS}}(mT_s)]\cos\theta_T + \cos\theta_p \sin\theta_T}\right\} \\
&\theta^A_{\mathrm{MCS}}(mT_s) \\
&\quad = \arccos\left\{-\sin\theta_p \cos[\phi_{\mathrm{MCS}}(mT_s)]\sin\theta_T + \cos\theta_p \cos\theta_T\right\}
\end{aligned} \tag{3}$$

where the superscript A indicates these angles are relative to the antenna. Thus, to maintain the beam pointed at the desired earth-relative scan angle $(\phi_p,\ \theta_p)$, expressions (3) should be used to determine the electronic steering angles.

B. Theoretical Analysis

It is of interest to study the effects of varying resolution volume locations and sizes introduced by the copolar antenna patterns when using MCS on radar-variable estimates. The size of the resolution volume is determined by the beamwidth, which is a function of steering angle in PARs, and the range resolution which is considered constant in this work. First, we investigate the effects of resolution volume locations on signal power estimates. Then, we investigate biases (i.e., with respect to the broadside beam of a stationary PAR) in copolar correlation coefficient as a function of resolution volume sizes. This accounts for: 1) impacts from the varying two-way radiation pattern beamwidths for pulses within the CPI and 2) impacts from beam pointing offsets that could be caused by a number of reasons (e.g., quantization of steering angles, phase noise, precision of the mechanical platform). It is assumed herein that biases in radar-variable estimates resulting from MCS are dominated by the mainlobe of the copolar radiation patterns in H and V.

The normalized one-way electric field antenna patterns as a function of steering angle can be described as [24]

$$F_i(\phi,\theta) = \sqrt{g_i(\phi_s,\theta_s)}\, f_i(\phi,\theta) \tag{4}$$

where $f_i(\phi,\theta)$ is the normalized one-way electric field antenna pattern, $g_i(\phi_s,\theta_s)$ is the one-way normalized power gain of the element pattern, and i is either "H" or "V" to indicate polarization. For system design purposes, it is common practice to assume that the scan loss from a planar array has a $\cos^{3/2}(\theta_s)$ (when the antenna is lying on the xy plane) dependence [16], hence

$$g_i(\phi_s,\theta_s) = \cos^{3/2}(\phi_s)\cos^{3/2}(\theta_s) \tag{5}$$

where $(\phi_s,\ \theta_s)$ are the steering angles relative to broadside in the antenna coordinate system (as shown in Fig. 3). For simplicity, axially symmetric Gaussian functions are used to model the mainlobe of copolar H and V radiation patterns [6]. This is without loss of generality because the most significant contributor to the biases being modeled is the mainlobe peak. So, whereas practical PAR patterns may not exactly follow a Gaussian beam model, in this context, the impacts of deviations from such model are very small. Since MCS operates mostly in ϕ, changes in θ (within the CPI) are ignored so this dimension is dropped to simplify the notation. Assume that the standard deviation of the Gaussian patterns is σ_h and σ_v, and that the difference in pointing direction is Δ_ϕ. Note that pointing offsets could come from many sources (e.g., phase shifters or mechanical bias) and therefore Δ_ϕ is treated here as a uniformly distributed random variable. Then, the power-normalized one-way power pattern of the mainlobe

electronically steered at ϕ_s can be expressed as [6] (C.16)

$$f_h^2(\phi) = \frac{1}{2\sigma_h\sqrt{\pi}} \exp\left[-\frac{(\phi-\phi_s+\Delta_\phi/2)^2}{4\sigma_h^2}\right] \quad (6)$$

$$\text{and } f_v^2(\phi) = \frac{1}{2\sigma_v\sqrt{\pi}} \exp\left[-\frac{(\phi-\phi_s-\Delta_\phi/2)^2}{4\sigma_v^2}\right]. \quad (7)$$

These widths are proportional to the HPBWs in H and V, and are expressed as $\sigma_i^2 = \phi_{1i}^2/16\ln 2$ [6], where ϕ_{1i} is the HPBW in ϕ and "i" is either "H" or "V." Furthermore, PAR beamwidth variations as a function of steering angle (relative to the array broadside) can be approximated by [16]

$$\phi_{1i}(mT_s) \approx \frac{\phi_{1i}(0)}{\cos[\phi_s(mT_s)]} \quad \text{and} \quad \theta_{1i}(mT_s) \approx \frac{\theta_{1i}(0)}{\cos[\theta_s(mT_s)]} \quad (8)$$

where $\phi_{1i}(0)$ and $\theta_{1i}(0)$ are the broadside beamwidths in ϕ and θ, respectively. This expression indicates that when using MCS, volume sizes for every pulse in the CPI are slightly different and the change is approximately proportional to $[\cos(\phi_s)\cos(\theta_s)]^{-1}$. Note that this change is negligible for small values of ϕ_s and θ_s.

Of interest is to compute signal power estimate as a function of steering angle and for the copolar antenna pattern functions adopted. The signal power estimate is computed as the average of M instantaneous signal-power samples. We assume a point target located in the center of the volume corresponding to the middle sample to obtain an upper bound on the largest biases from varying resolution-volume locations. Assuming a high signal-to-noise ratio (SNR) such that the impact of the receiver noise can be considered negligible (i.e., SNR $\geq$ 20 dB)

$$\begin{aligned}\frac{\hat{P}_h}{P_h} &\triangleq \frac{1}{M}\sum_{m=0}^{M-1}|V_h(mT_s)|^2 - N_h \\ &\approx \frac{1}{M}\sum_{m=0}^{M-1}|V_h(mT_s)|^2 \approx \cdots \\ &\cdots \approx \frac{1}{M}\sum_{m=0}^{M-1}\int_{\phi,\theta}|F_h(\phi_m)|^4 d\phi \end{aligned} \quad (9)$$

where $\hat{P}_h$ and $V_h(mT_s)$ are the signal power estimate in H and the received complex voltage for the horizontal polarization, respectively. Then, using (4) and (5) with $g_i(\phi_s, \theta_s)$ expressed as a function of time as in (8), (6), σ_h as a function of $\phi_{1h}(mT_s)$, into (9)

$$\hat{P}_h = \frac{1}{M}\sum_{m=0}^{M-1} g_h(mT_s)^2 \frac{2}{\phi_{1h}(mT_s)}\sqrt{\frac{\ln\ (2)}{\pi}}\cdots \\ \cdots \int_\phi \exp\left\{-\frac{\left[\phi-\phi_s(mT_s)+\Delta_\phi(m)/2\right]^2}{\phi_{1h}^2(mT_s)/2\ln 2}\right\} \quad (10)$$

where $\phi_s(mT_s)$, $g_h(mT_s)$, and $\phi_{1h}(mT_s)$ are the steering angle, the power gain for the H polarization, and the HPBW as a function of sample number, respectively. Note that Δ_ϕ is a function of m. The bias of power estimates (with respect to the broadside and with no antenna motion) is computed as

$$\frac{\delta P_h}{P_h} = 1 - \frac{\hat{P}_h}{P_h} = 1 - \frac{1}{M}\sum_{m=0}^{M-1} g_h(mT_s)^2 \cdots\cdots \frac{2}{\phi_{1h}(mT_s)} \\ \times \sqrt{\frac{\ln\ (2)}{\pi}}\int_\phi \exp\left\{-\frac{\left[\phi-\phi_s(mT_s)+\Delta_\phi(m)/2\right]^2}{\phi_{1h}^2(mT_s)/2\ln 2}\right\}. \quad (11)$$

For a constant ϕ_s, this expression represents the bias of power estimates from an RPAR scanning a fixed electronic beam pointed at ϕ_s. In particular for $\phi_s = 0°$, it represents the bias introduced by sampling slightly shifted uniform resolution volumes, as in the conventional scan of a reflector-antenna radar. Similarly, selecting $\phi_s(mT_s) = \phi_{\text{MCS}}^A(mT_s)$ in (3) provides an expression for the bias in power estimates arising from the changes in copolar patterns of the RPAR scanning when using MCS. Note that (11) accounts for the scan loss (i.e., gain variations as a function of steering angle) as well as the change in volume size as a function of sample.

The estimator for the copolar correlation coefficient, ρ_{hv}, in the simultaneous transmit simultaneous receive (STSR) mode is defined as [25]

$$\hat{\rho}_{hv} = \frac{\left|\frac{1}{M}\sum_{m=0}^{M-1} V_h^*(mT_s)V_v(mT_s)\right|}{\sqrt{\hat{P}_h\hat{P}_v}} \quad (12)$$

where $V_v(mT_s)$ and $\hat{P}_v$ are the echo voltage and estimated signal power in V, respectively. For the following analysis, assume that resolution volumes are homogeneously filled with identical scatterers so that in case of perfectly matched beams in width and pointing direction, the true copolar correlation coefficient is equal to ρ_{hv}, despite the changes in size and location of resolution volumes in an MCS CPI. That is, we are focusing on the impacts of imperfect matching between the H and V patterns. The bias of ρ_{hv} due to copolar mainlobe differences between the H and V polarizations is given by [26]

$$\delta\rho_{hv} = \rho_{hv}\frac{1}{M}\sum_{m=0}^{M-1}\left[\frac{\int_{\phi,\theta}F_h^2F_v^2}{\sqrt{\int_{\phi,\theta}F_h^4\int_{\phi,\theta}F_v^4}} - 1\right]. \quad (13)$$

The integrals in (13) are 2-D over the hemispheric solid angle defined by ϕ and θ. A closed-form expression can be derived for the case of interest (i.e., narrow beams) using (4)–(7)

$$\frac{\int_{\phi,\theta}F_h^2F_v^2}{\sqrt{\int_{\phi,\theta}F_h^4\int_{\phi,\theta}F_v^4}} = \frac{2\phi_{1h}\phi_{1v}}{\phi_{1h}^2+\phi_{1v}^2}\exp\left[-\frac{4\Delta_\phi^2\ln\ (2)}{\phi_{1h}^2+\phi_{1v}^2}\right] \quad (14)$$

and then inserting into (13) to get

$$\delta\rho_{hv} = \rho_{hv}\frac{1}{M}\sum_{m=0}^{M-1}\left\{\frac{2\phi_{1h}\phi_{1v}}{\phi_{1h}^2+\phi_{1v}^2}\exp\left[-\frac{4\Delta_\phi^2\ln\ (2)}{\phi_{1h}^2+\phi_{1v}^2}\right]-1\right\}. \quad (15)$$

The dependence of ϕ_{1h} (and θ_{1h}) with sample time is dropped to simplify notation, but it is emphasized that beamwidths are a function of sample time as described by (8). Similarly, it is emphasized that each realization (m) results in a different value of Δ_ϕ, although this is not explicit in the

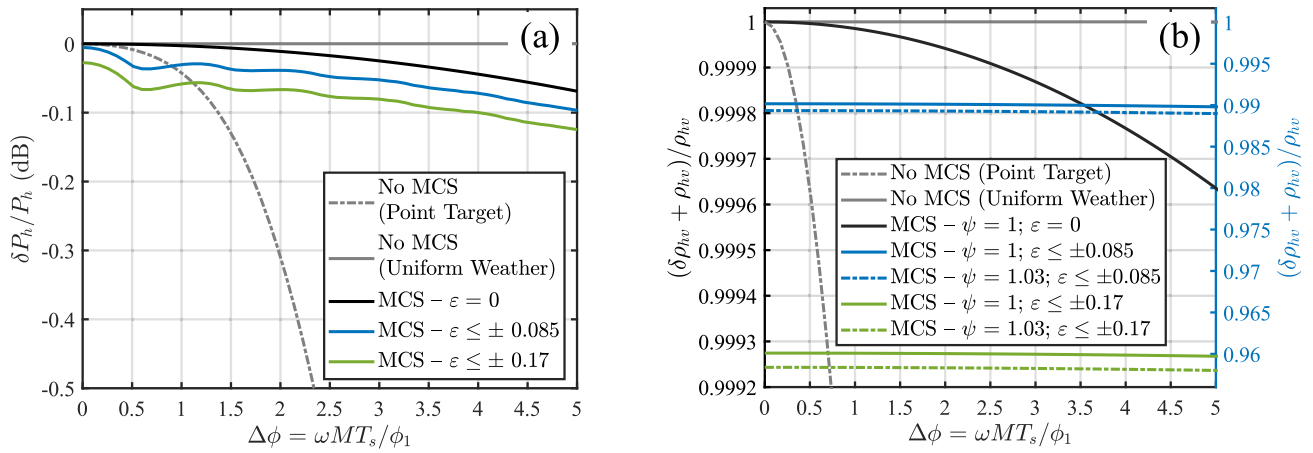

Fig. 4. Biases in (a) signal power and (b) correlation coefficient due to copolar mainlobe differences within the CPI estimated using (11) and (15). Note that for (b) the left ordinate axis (in black) is used for the ideal cases (i.e., $\varepsilon = 0$ and $\psi = 1$) and the right one (in blue) for all others.

expression. A quick check of this expression indicates that, for zero beam offset and equal beamwidths in H and V, $\delta\rho_{hv} = 0$. In deriving (15), it is implicitly assumed that the antenna beams are circular ($\phi_{1h} = \theta_{1h}$). For elliptical beam patterns, which represent the more general shapes of H and V beams of a PAR, the pertinent equation (15) becomes

$$\delta\rho_{hv} = \rho_{hv}\frac{1}{M}\sum_{m=0}^{M-1}\left\{\begin{array}{l}\dfrac{2\phi_{1h}\phi_{1v}}{\phi_{1h}^2+\phi_{1v}^2}\exp\left[-\dfrac{4\Delta_\phi^2\ln(2)}{\phi_{1h}^2+\phi_{1v}^2}\right]\times\cdots \\ \cdots\dfrac{2\theta_{1h}\theta_{1v}}{\theta_{1h}^2+\theta_{1v}^2}\exp\left[-\dfrac{4\Delta_\theta^2\ln\ (2)}{\theta_{1h}^2+\theta_{1v}^2}\right]-1\end{array}\right\} \tag{16}$$

where Δ_ϕ and Δ_θ are offsets in ϕ and θ, and are uniformly distributed random variables in sample time.

For illustration, assume that beamwidths in H and V are matched ($\phi_{1h} = \phi_{1v}n$) in (15), but there is an offset in beam-pointing directions ($\Delta_\phi \neq 0$), as follows:

$$\Delta_\phi \leq \pm\varepsilon\phi_{1v} \tag{17}$$

where ε is an upper bound on the beam pointing offset normalized to the beamwidth, which is assumed to be much smaller than 1. Inserting these conditions into (15), and assuming that the pointing offset causes reduction of the correlation, we arrive at

$$\chi \triangleq \frac{\delta\rho_{hv}+\rho_{hv}}{\rho_{hv}} \leq \exp\left[-2\ln(2)\varepsilon^2\right] \tag{18}$$

which represents a correlation reduction factor due to a beam pointing mismatch $\Delta_\phi \leq \pm\varepsilon\phi_{1h}$. Next, solving (18) for ε leads to

$$\varepsilon \leq \pm\sqrt{-\frac{1}{2\ln\ (2)}\ln(\chi)}. \tag{19}$$

This expression can be used to determine the maximum pointing offset between H and V that is allowed for a required bias in ρ_{hv}. For example, for the required bias[2] of 0.01, a $\chi \geq 0.99$ results in $|\varepsilon| \leq 0.085$. And for a beamwidth of $\sim$1°, $|\Delta_\phi| \leq 0.085°$. Considering the demanding requirement on the bias of ρ_{hv}, which is very sensitive to measurement errors, it is expected that this pointing accuracy should be sufficient to achieve similar requirements for other polarimetric variables, although polarimetric measurements of differential phase and linear depolarization ratio are also extremely sensitive to errors and mismatches. A detailed theoretical analysis of the required pointing accuracy for other polarimetric variables is beyond the scope of this article and is left for future research. This important result has to be considered in the design of the RPAR; as will be discussed in Section II-C, the choice of phase shifters will impact the achievable accuracy of ρ_{hv} estimates. Another important aspect that needs to be considered is the mismatch of H and V beamwidths, which is conveniently represented by their ratio, defined here as $\psi = \phi_{1h}/\phi_{1v}$.

Biases in signal power and correlation coefficient due to copolar mainlobe differences within the CPI estimated using (11) and (15) are shown in Fig. 4 as a function of the normalized azimuthal sampling $\Delta\phi$, and for different values of ε and ψ. To provide bounds on the performance of MCS with respect to scanning with no beam steering (e.g., a mechanical scanning antenna), we have included the point target and uniform weather target biases resulting from no MCS. Fig. 4(a) shows that for the case with no beam steering (referred to as "No MCS" in Fig. 4), signal power estimates are unbiased for a uniform weather target (i.e., constant reflectivity), and are negatively biased for a point target (i.e., can be thought of as a very large gradient of reflectivity). Considering that actual precipitation does not have perfectly uniform nor point target characteristics, the biases for the case with no beam steering lie between these two curves. Considering the MCS performance for zero beam offset (i.e., $\varepsilon = 0$), there is a small negative bias (<0.1 dB) in signal power estimates. Note that for the $\Delta\phi$ typically used in WSR-88D VCPs (i.e., 0.5 or 1), this bias is insignificant (<0.0025 dB). For a uniformly distributed offset with $|\varepsilon| \leq 0.085$, the power bias from MCS is comparable to that resulting for the point target case with no beam steering up to $\Delta\phi \sim 1$, and lower for $\Delta\phi > 1$. A similar conclusion can be drawn from the case when ε is twice that value (i.e., $|\varepsilon| \leq 0.17$). For all MCS cases in Fig. 4(a), biases are small and well within the reflectivity data-quality requirements. Fig. 4(b) shows that with zero beam offset

[2]Specified in the NOAA Radar Functional Requirements document p. 13.

(i.e., $\varepsilon = 0$) and perfectly matched beamwidths (i.e., $\psi = 1$), the bias in ρ_{hv} from MCS is negligible ($\delta\rho_{hv} < 0.0004$), while the estimates when scanning with no beam steering are unbiased for a uniform weather target. As expected, the negative bias in ρ_{hv} for the point-target case and with no beam steering increases rapidly. This case is included for completeness, but since ρ_{hv} has meaning only in the context of weather observations, the point-target curve is not discussed further. Note that the left ordinate axis (in black) is used for the no-beam-steering and ideal MCS (i.e., $\varepsilon = 0$ and $\psi = 1$) cases and the right axis (in blue) for all others. For a uniformly distributed ε, with $|\varepsilon| \leq 0.085$, and $\psi = 1$ or $\psi = 1.03$, the expected bias is $\delta\rho_{hv} \sim 0.01$ (as designed with $\chi = 0.99$), and there is little-to-no dependence with the normalized azimuthal sampling. Similarly, for $|\varepsilon| \leq 0.17$, and $\psi = 1$ or $\psi = 1.03$, $\delta\rho_{hv} \sim 0.04$. It is apparent from these curves that the differential beam pointing offsets considered have a larger impact on ρ_{hv} estimates than a 3% mismatch ($\psi = 1.03$) in H and V beamwidths, although the impact of the same beam mismatch is larger as the pointing offset increases. In summary, these results show that for relatively accurate beam pointing (i.e., $|\Delta_\phi| \leq 0.085\phi_{1h}$), MCS achieves the required data quality on signal power and correlation coefficient estimates, but it would result in unacceptable data quality degradations for larger pointing offsets (e.g., $|\Delta_\phi| > 0.085\phi_{1h}$). We note that it is generally not possible to use these results to correct for the biases, because these biases depend on the instantaneous beam pointing offset (i.e., pulse to pulse) and the actual weather signal characteristics, which are unknown in the typical weather surveillance operation.

C. MCS Concept of Operations

It is of interest to define two CONOPS that use the MCS technique. Provided that the beam pointing offset is sufficiently small (e.g., $\Delta_\phi \leq \pm 0.085\phi_{1h}$) and that the H and V beams are adequately matched (i.e., $\phi_{1h} \approx \phi_{1v}$), MCS could improve azimuthal resolution without impacting the quality of radar-variable estimates. Two alternatives are presented along with tradeoff considerations associated with each CONOPS. Both CONOPS discussed in this subsection were implemented on the ATD system and are demonstrated in Section IV.

1) Broadside MCS: A straightforward implementation of MCS can be achieved by using (3) with $\phi_p = 0°$ and $\theta_p = 90° - \theta_{el}$. For illustration, assume the antenna is not tilted (i.e., $\theta_T = 0°$) and θ_{el} is a small angle (e.g., 0.5°) such that $\sin(\theta_p) \approx 1$ and $\cos(\theta_p) \approx \theta_p$, which reduces (3) to

$$\phi^A_{\text{BMCS}}(mT_s) = \omega T_s \left[\frac{(M-1)}{2} - m\right]$$
$$\theta^A_{\text{BMCS}}(mT_s) = \theta_p \tag{20}$$

where the subscript indicates *broadside* MCS (BMCS). This expression provides the electronic steering angles for transmitted pulses within the CPI defined by M and T_s, and it results in a normalized azimuthal sampling of $\Delta\phi = \omega M T_s/\phi_1$. That is, as the RPAR rotates, motion is compensated by the steering angles in (20) such that all resolution volumes defined by samples in each CPI are centered at $\phi_k = k\ (\omega M T_s)$ where $k \in \{0, 1, 2, \ldots\}$ and it represents a CPI index number.

TABLE I
FB-MCS CONOPS

Scan \ Beam	Forward-Looking	Back-Scanning
M	3	61
T_s	3 ms	1.48 ms
ϕ_p	+10°	-10°
Received Beams	5	1

There are a couple of major advantages of this CONOPS. First, since the steering angles are relatively small and remain close to the antenna's principal planes, it is expected that a simple broadside calibration (i.e., similar to that of a rotating reflector-antenna radar) will be sufficient for the required accuracies of radar-variable estimates. Second, considering that the set of pointing angles resulting from (20) for a predefined CPI are deterministic, this results in an invariant scan strategy that mitigates beam-smearing effects with negligible data quality impact, and does not require additional signal processing for implementation.

Nevertheless, the simplicity of this CONOPS imposes some constraints on the effective use of the RPAR's resources to meet the prescribed functional requirements. That is, while this simple CONOPS may mitigate beam-smearing effects (which results in a smaller required antenna aperture), it does not support achieving other demanding functional requirements such as the quality of radar-variable estimates. A more advanced MCS CONOPS that could support improved data quality is discussed next.

2) Forward-Looking and Back-Scanning MCS: The CONOPS discussed here uses a scan strategy based on *forward-looking* and *back-scanning* MCS (FB-MCS) beams. Forward-looking beams consist of short-dwell CPIs for which the steering angles are ahead of the radar rotation and are designed to provide *sufficient* surveillance information about upcoming potential regions of interest. Back-scanning beams consist of longer dwell CPIs for which steering angles are less than or equal to those from forward-looking beams and are designed to provide high-quality weather observations. In the FB-MCS CONOPS, CPIs of FB beams are interleaved. The concept is illustrated in Fig. 5, where a top view of the RPAR shows a wide *spoiled* transmit beam used for the forward beams (black pattern) and a narrow *pencil* beam used for the back-scanning beams (blue pattern). Digital beamforming is coupled with forward-looking beams to increase the coverage of these quick surveillance beams by transmitting a spoiled beam in azimuth and receiving multiple simultaneous beams [27]. MCS beam-pointing angles for these beams are derived using (3). An example set of scan parameters that interleaves FB beams is summarized in Table I.

In conjunction with the FB-MCS CONOPS, the RPAR's beam agility can be used to focus the scan in regions of interest within the visible region (e.g., typically ±45° from broadside) as the radar rotates. This is an example of *adaptive scanning*, by which the scan strategy dynamically evolves to

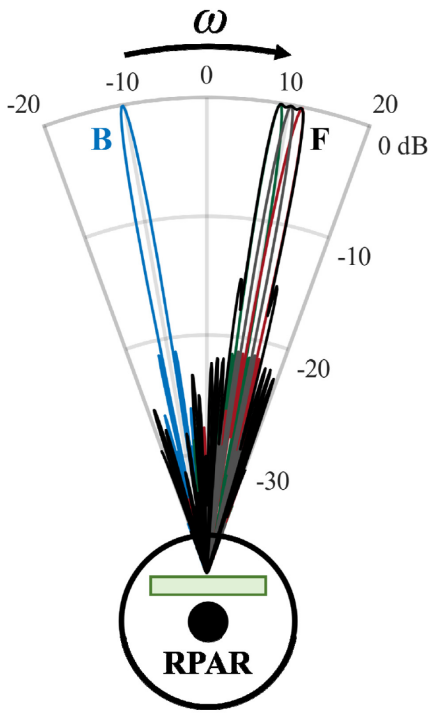

Fig. 5. FB-MCS CONOPS. The solid black circle represents center of rotation and the green rectangle represents the PAR antenna.

make efficient use of the radar resources observing regions of interest [12]. The back-scanning beams considered in this work are deterministically scheduled but could conceptually be scheduled adaptively. That is, using information from the forward-looking beams, the back-scanning beams can be defined (i.e., beam positions and dwell times) to tailor the observations on significant weather echoes. For example, the maximum range of storms could be computed from the forward-looking beams, and the CPIs of the back-scanning beams could be designed to match these maximum ranges. While the PRTs of the backward beams are reduced (to match the maximum range of storms), the number of samples would be increased to approximately maintain the dwell time. This would lead to improved radial velocity and spectrum width estimates (due to the extended Nyquist co-interval), more effective mitigation of ground clutter contamination, and to a reduction in the variance of estimates (due to the increased number of samples). MCS would be especially beneficial for scheduling back-scanning beams to maximize the use of radar resources with the goal of improving weather observations and meeting functional requirements. This potential application of the FB-CONOPS is presented here to motivate the use of MCS at off-broadside steering angles. An adaptive implementation of the FB-MCS CONOPS is beyond the scope of this work and will be considered for future research.

III. Performance of MCS

High-fidelity RPAR simulations were developed to evaluate the performance of MCS to enhance azimuthal resolution, and to quantify its impact on the bias of polarimetric-variable estimates. One set of simulations is used to evaluate the performance of MCS on enhancing azimuthal resolution (i.e., decrease the effective beamwidth); these are designed to quantify the importance of beam pointing accuracy to achieve a significant reduction in the effective beamwidth. The other set of simulations is used to quantify the impact of MCS on data quality; these are designed to capture the combined effects of sampling concentric nonuniform resolution volumes and antenna radiation patterns. Data produced with both sets of simulations are compared to RPAR simulations that do not use MCS as well as to PAR operation in a stationary mode.

A. Azimuthal Resolution

As argued before, the performance of MCS could have important implications in the size of the antenna aperture needed to meet angular-resolution requirements. That is, as illustrated in Fig. 1, an antenna aperture with a stationary beamwidth of 1° on broadside results in a ∼1.23° effective beamwidth when sampling at $\Delta\phi = 1$. Thus, an aperture with a stationary beamwidth of 0.8° on the broadside is needed for an effective beamwidth of 1° at $\Delta\phi = 1$. However, this can result in a significant increase in aperture size (e.g., $N_{1^\circ} = 11,700$ to $N_{0.8^\circ} = 18,100$), which would increase system complexity and cost. The use of MCS could result in a reduction of the effective beamwidth, thus potentially reducing system cost. It is important to note that the performance of MCS to enhance the RPAR's angular resolution is mostly controlled by beam-pointing accuracy (determined by the pointing offset Δ_ϕ) and knowledge of the platform's mechanical position.

The beam pointing accuracy of a phased array antenna is dictated by the performance of phase shifters in the antenna elements [28]. Phase shifters control the phase of the signals at each radiating element to electronically form a collimated beam in the desired direction. A digitally controlled phase shifter with n bits has 2^n phase states separated by phase steps of $2\pi/(2^n)$ [16]. This phase quantization introduces an error in the steering phase at the element level and may cause a distortion of the resulting antenna pattern. Two major adverse effects from phase quantization have been the subject of several research efforts: increase in antenna sidelobe levels and beam-pointing accuracy [29].

Phase quantization errors are predictable and are typically considered in the design of phased array antennas. Nevertheless, imperfections in antenna fabrication and other sources of error (e.g., differences in the power divider network, failed bits in phase shifters, mutual coupling between elements, and thermal noise) introduce random phase errors that are well approximated by a Gaussian probability density function with zero mean [16], [30], [31]. These random phase fluctuations have to be considered to quantify the impact of beam pointing accuracy as a function of n on the effective beamwidth achieved by MCS. The simulation developed for this analysis includes phase quantization errors and also random phase errors. Random amplitude fluctuations generated from a Gaussian distribution with a standard deviation of −6 dB, which are characteristic of the real antenna hardware [23], were also introduced to model elements failures across the array.

The transmit and receive antenna patterns are generated as the product of a measured embedded element pattern and a simulated array factor [16]. The array factor is generated using the Fourier method. The measured embedded element pattern[3] is used to enhance the fidelity of simulations and corresponds to that of an element designed for the ATD system [32]. Steering phases at the element level are produced by quantizing Gaussian random variables with a mean equal to the desired quantized steering phase (rounded to the nearest bit as a function of n) and a standard deviation of 5° [16]. As is done conventionally, transmit patterns are generated with a uniform taper to maximize sensitivity and receive patterns are tapered with a Taylor window to reduce sidelobe levels. This simulation captures the systematic and random phase errors and includes effects from both copolar and cross-polar antenna radiation patterns.

The procedure described is used to simulate M patterns steered in ϕ using MCS as described in (2). Without loss of generality, ϕ_p is assumed to be 0°, which corresponds to BMCS. Results can be scaled by $1/\cos(\phi_p)$ for the effective beamwidth at a pointing angle $\phi_p \neq 0$. RPAR rotation is simulated by shifting each pattern in ϕ by $-\omega m T_s$, which assumes a uniform antenna rotation rate in azimuth. The effective antenna pattern is obtained by adding these M patterns, from which the effective beamwidth is measured. Results for $n = 5$, 6, and 7 bits are presented in Fig. 6 as a function of the normalized azimuthal sampling $\Delta\phi$. It is apparent from the results in Fig. 6(a) that due to phase errors (dominated by quantization errors), 5-bit phase shifters are not sufficient to mitigate beam-smearing effects considerably. In this case, an antenna aperture with a stationary beamwidth of 1° on broadside results in a ∼1.20° effective beamwidth when sampling at $\Delta\phi = 1°$. This indicates that the pointing offset for $n = 5$ was relatively large and the centers of resolution volumes could not be aligned with the required precision. The effective beamwidth was greatly reduced with $n = 6$, as shown in Fig. 6(b). While not completely mitigated, beam-smearing effects are largely reduced with 6-bit phase shifters, being the effective beamwidth within 0.1° from the stationary beamwidth for all N and all $\Delta\phi$. Lastly, Fig. 6(c) indicates that for $n = 7$ beam-smearing effects are negligible and the effective beamwidth is approximately equal to the stationary beamwidth.

Results presented here quantify the performance of MCS in enhancing angular resolution by mitigating beam-smearing effects as a function of phase shifter bits. It is expected that 6-bit phase shifters [Fig. 6(b)] are sufficient for achieving good MCS performance, while 7-bit phase shifters would be ideal.

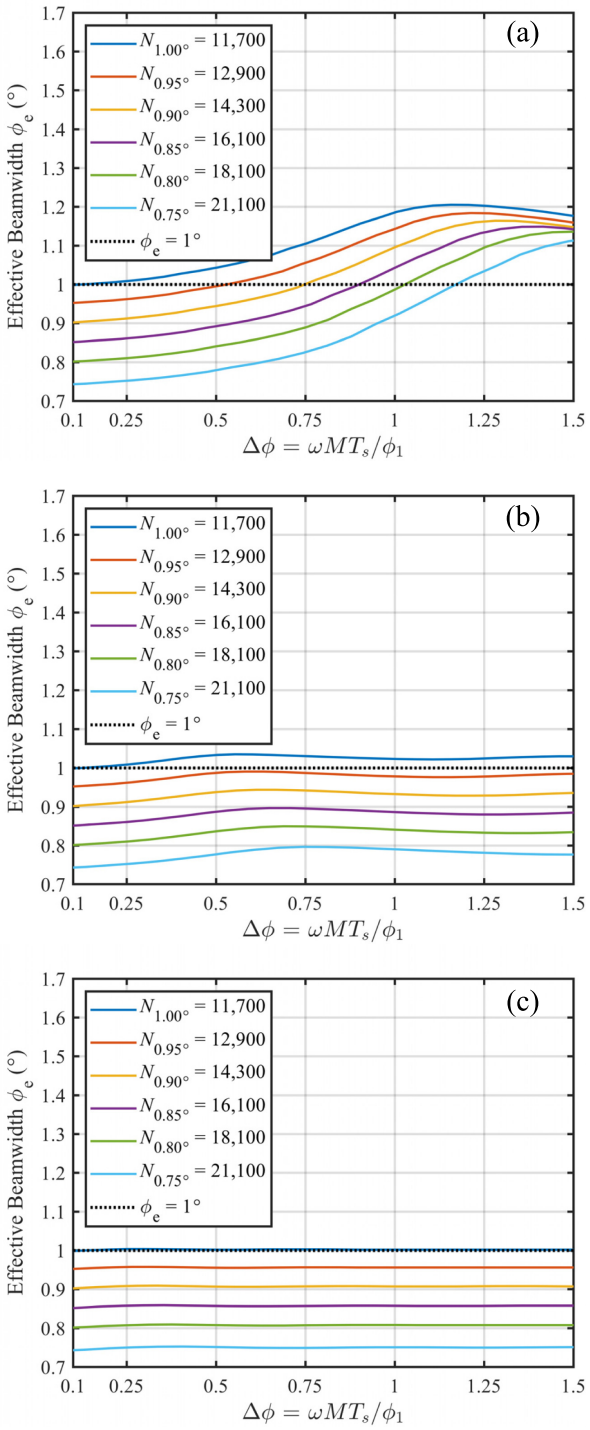

Fig. 6. Effective beamwidth as a function of the normalized azimuthal sampling $\Delta\phi$ for (a) $n = 5$, (b) $n = 6$, and (c) $n = 7$ phase shifter bits. The stationary beamwidth for all cases is for the broadside position.

B. Data Quality

The simulations used to evaluate the impact of MCS on data quality are based on the approach proposed by Ivić [33], which combines the effects of simulated or measured radiation patterns with simulated time-series signals. It applies the well-established backscattering matrix model [23], [24] that includes bulk statistical properties of scatterers within a resolution volume over the dwell time coupled with electromagnetic wave propagation and radar system effects. In addition to the copolar biases quantified in Section II-B, the simulation can be used to quantify the effects from both the copolar and cross-polar antenna radiation patterns. The present work considers copolar antenna patterns only.

[3]Measurements were obtained in the near-field chamber at the Massachusetts Institute of Technology (MIT) Lincoln Laboratory facilities during March–April 2018.

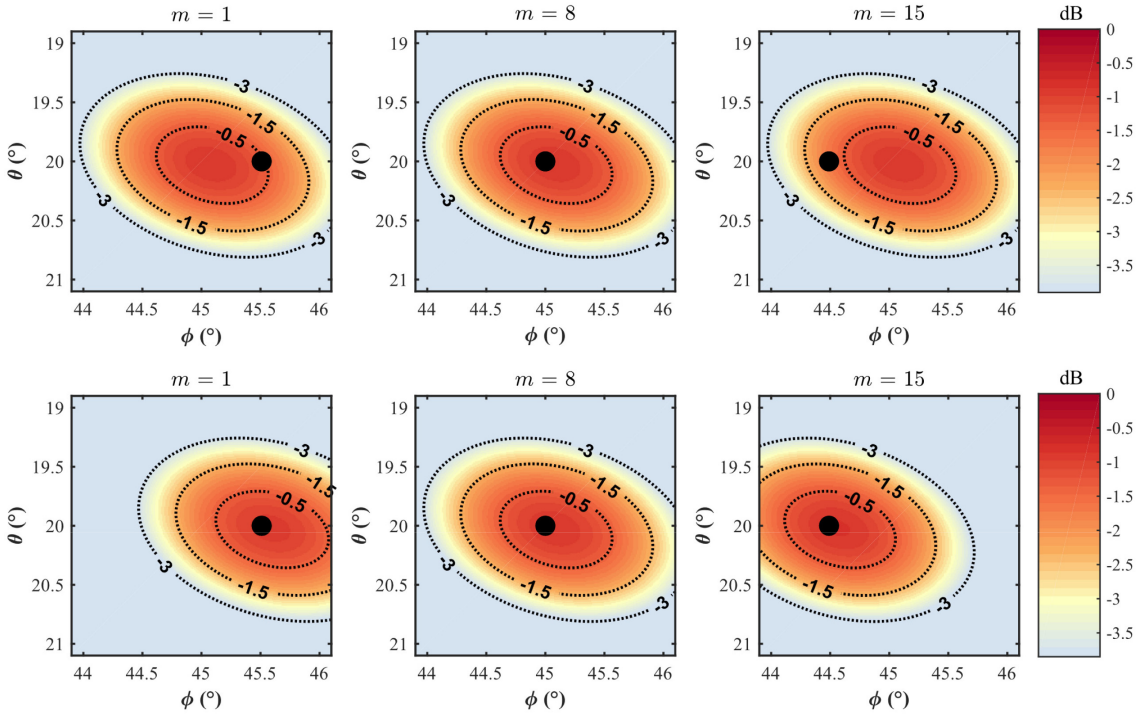

Fig. 7. Copolar beam peaks for the transmit antenna pattern of the simulated RPAR pointed at $\phi_{az} = 45°$ and $\theta_{el} = 20°$, with a rotation rate of $\omega = 21.15°$ s^{-1}, $M = 15$, and $T_s = 3$ ms. (Top row) Beam peaks corresponding to constant beam steering for samples $m = 1$, 8, and 15. (Bottom row) Beam peaks corresponding to MCS for the same samples. The black dot represents the desired pointing angle ϕ_{az} and θ_{el} (earth-relative coordinates), which is constant in earth-relative coordinates for the duration of the CPI.

The RPAR simulation procedure is similar to that discussed in Section III-A. A set of M simulated transmit and receive patterns are steered in ϕ using MCS as described in (2), and rotation is simulated by shifting each pattern in ϕ by $-\omega m T_s$. The two-way patterns are sampled at the desired pointing angle ϕ_p and θ_p for every m. It is assumed that the pointing angle (relative to the earth coordinate system) is constant for the duration of the CPI, and that steering angles for simulated patterns may change as a function of sample m. RPAR simulations for the case where constant beam steering is used (i.e., no MCS) are also generated for reference using the same procedure. An illustration of the copolar transmit beam peaks resulting from this simulation procedure is shown in Fig. 7, where the beam pointing angle is $\phi_{az} = 45°$ and $\theta_{el} = 20°$ ($\phi_{az} = \phi_p$, and $\theta_{el} = 90° - \theta_p$), the rotation rate is $\omega = 21.15°$ s^{-1}, $M = 15$, and $T_s = 3$ ms. The top row shows the beam peaks with constant beam steering (i.e., no MCS) as a function of steering angle relative to the array broadside for samples $m = 1$, 8, and 15, while the bottom row is analogous but using MCS. Note that since the steering angle for this example is far from the broadside, there is a scan loss of ∼1 dB. Black dotted lines delineate contour levels of constant power with respect to the beam peak (in dB). The black dot represents the desired pointing angle ϕ_{az} and θ_{el}, which is constant in earth-relative coordinates for the duration of the CPI. It can be observed in the top-left ($m = 1$) and top-right ($m = 15$) panels that the beam is not accurately pointed at the desired angle. For example, this would translate into a loss of ∼0.5 dB in power if scanning a point target. Although this would generally have little impact on uniformly distributed weather targets, it could introduce biases in large reflectivity gradients such as those observed in tornado vortices. Applying MCS results in more accurate pointing and a negligible power loss (with respect to the peak of the pattern) due to the pointing offset. The complex samples obtained from two-way patterns at the desired pointing angle are used in the backscattering matrix model, which includes statistical properties of meteorological scatterers. This generates the simulated time series of complex voltages, from which spectral moments and polarimetric variables are estimated.

To understand the impact of MCS on the quality of variables using the described simulation procedure over the scan volume, the space of pointing angles $\phi_{az} \in [-45°, 45°]$ and $\theta_{el} \in [0°, 20°]$ is simulated, with a grid spacing for both ϕ_{az} and θ_{el} of 1°. As before, constant beam steering is simulated for reference over the scan sector. It represents an RPAR scanning with a set of M identical electronic beams steered a constant angle (in the antenna-relative coordinate system) as the radar rotates. These simulations assume identical statistical properties for precipitation in the entire scan sector. Simulated weather signals are generated with an SNR of 20 dB, $\sigma_v = 2$ m s^{-1}, $Z_{DR} = 0$ dB, $\rho_{hv} = 1$, $M = 15$, and $T_s = 3$ ms. The simulated radial velocity and Φ_{DP} are arbitrarily set to 0 (m s^{-1} and °, respectively) since these do not impact the variables under consideration. Antenna characteristics based on the ATD system are adopted for this analysis since this system is used to demonstrate MCS in Section IV. This antenna is composed of 4, 864 radiating patch-antenna elements with dual

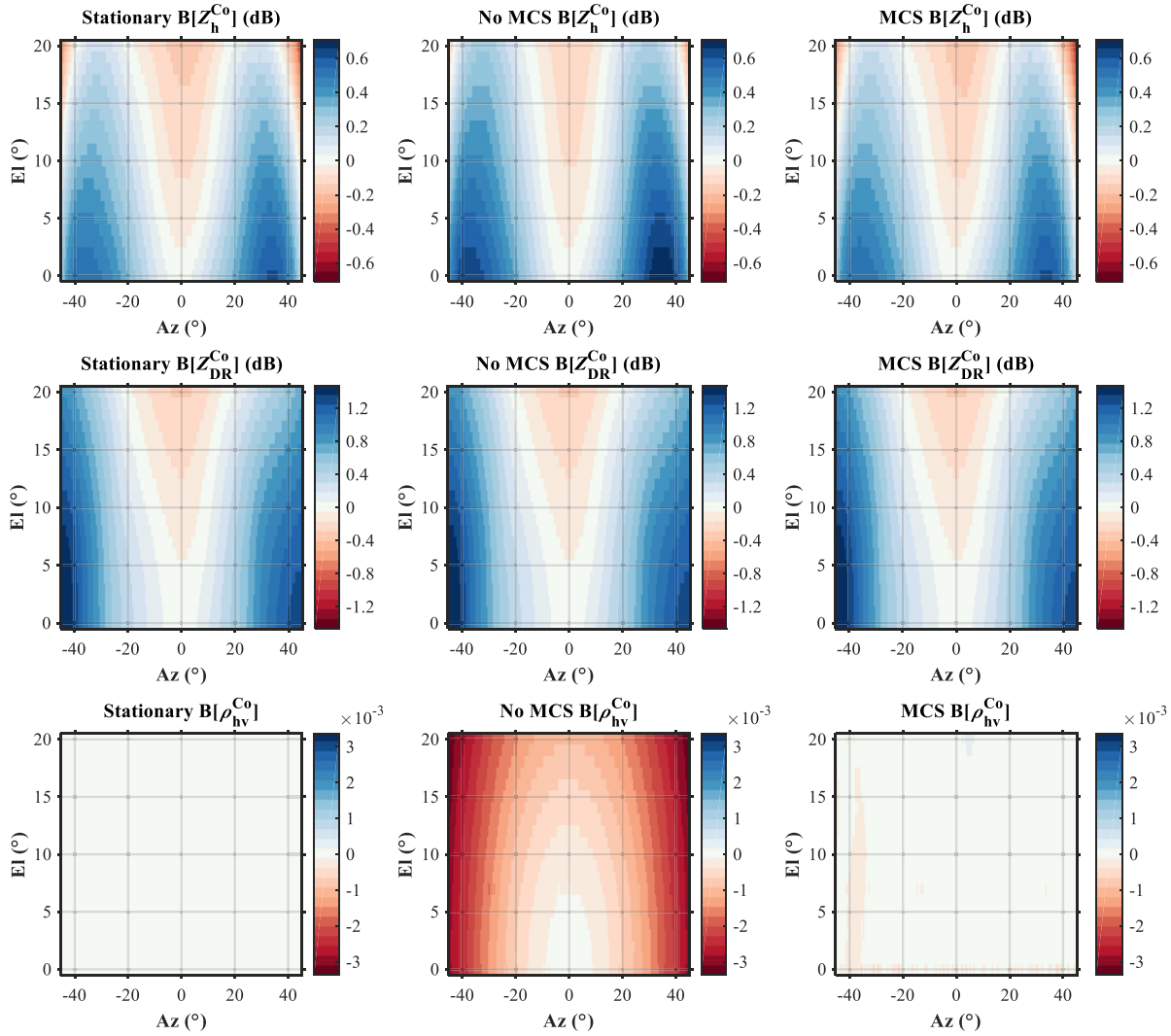

Fig. 8. Columns from left-to-right correspond to a stationary PAR, an RPAR not using MCS, and an RPAR using MCS, respectively. From top-to-bottom, the rows correspond to biases of Z_h, Z_{DR}, and ρ_{hv}. Absolute calibration constants for the broadside beam are derived from the stationary PAR for unbiased powers on both polarization channels (H and V) and applied to all three cases.

linear polarization (H and V). The arrangements of antenna elements in the ATD have been spaced by half wavelength which results in a $\sim 4 \times 4$ m^2 aperture that produces a $\sim 1.58°$ beamwidth on the broadside. Antenna elements are designed with 6-bit phase shifters. It is assumed that the antenna tilt angle is 0°, that is, the broadside is perpendicular to the z-axis.

Simulation results quantifying the copolar beam steering biases are presented in Fig. 8. Columns from left-to-right correspond to a stationary PAR, an RPAR not using MCS, and an RPAR using MCS, respectively. From top-to-bottom, the rows correspond to biases of reflectivity (Z_h), differential reflectivity (Z_{DR}), and ρ_{hv}. Absolute calibration constants for the broadside beam are derived from the stationary PAR for unbiased powers on both polarization channels (H and V) and applied to all three cases.

Comparing the results for Z_h on the first row, it is apparent that positive biases for the RPAR not using MCS are higher along the azimuth planes at $\sim \pm 38°$, with respect to both the stationary PAR and the RPAR using MCS. Negative biases along the azimuth plane at $\sim 0°$ are lower than those for the stationary PAR and the RPAR using MCS (specially at higher elevations). Comparing the results for Z_{DR} on the middle row, it is apparent that all three cases have very similar performance. To understand this, consider that Z_{DR} is the ratio of the H and V signal powers, each of which is estimated by averaging M signal power samples from potentially nonconcentric or nonuniform volumes. Volume locations or sizes for the H and V polarizations may change in a relatively similar manner as a function of steering angle. The resulting relative changes in signal powers from a set of M nonconcentric or nonuniform resolution volumes are thus similar, and differences cancel out in the ratio. Lastly, comparing the results for ρ_{hv} on the last row, it is apparent that estimates for the stationary PAR and the RPAR using MCS are unbiased, and there are small negative biases for the RPAR not using MCS.

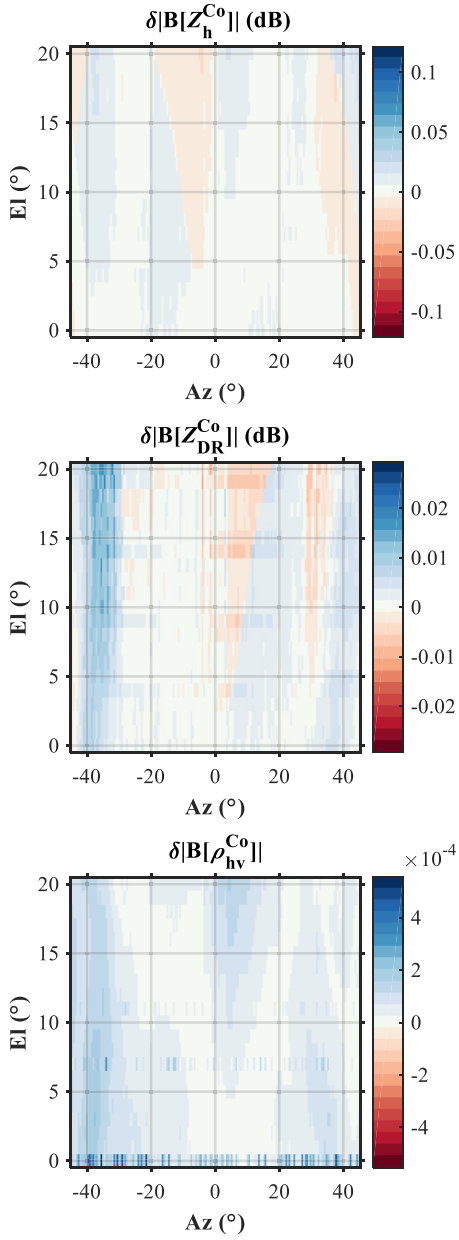

Fig. 9. Absolute bias differences between the stationary PAR and the RPAR using MCS (Top) Z_h, (Center) Z_{DR}, and (Bottom) ρ_{hv}. The $\delta|\mathrm{B}[\cdot]|$ notation is used to denote the difference in the absolute value of biases.

Biases for the RPAR not using MCS come from differences between the cross correlation power [the numerator in (12)] and the geometric mean of H and V signal powers. The bias magnitude for ρ_{hv} increases as a function of steering angle relative to the broadside, with unbiased estimates at $\phi_{az} \sim \pm 8°$ and $\theta_{el} = \sim 0° - 6.°$, and the largest biases in the scan sector at $\phi_{az} \sim \pm 45°$ and $\theta_{el} = 20°$. Nevertheless, the largest bias magnitudes obtained for the RPAR not using MCS are on the order of 0.003, which are small enough and meet the requirements for the weather surveillance mission [4].

Absolute bias differences between the stationary PAR and the RPAR using MCS are shown in Fig. 9. Panels from top-to-bottom correspond to differences in the absolute value of biases for Z_h ($\delta|\mathrm{B}[Z_h^{\mathrm{Co}}]|$), Z_{DR} ($\delta|\mathrm{B}[Z_{\mathrm{DR}}^{\mathrm{Co}}]|$) and ρ_{hv} ($\delta|\mathrm{B}[\rho_{hv}^{\mathrm{Co}}]|$), respectively. Notice that the color map scales are an order of magnitude smaller than the corresponding ones in Fig. 8. It is apparent from the top and center panels that biases of the stationary PAR and the RPAR using MCS for Z_h and Z_{DR} are very similar. The bottom panel shows that there may be small biases in ρ_{hv} for the RPAR using MCS in some areas of the scan sector, but these are negligible ($\sim 10^{-4}$) and are therefore ignored herein. These results show that a system designed with sufficient pointing accuracy can be operated as an RPAR using MCS, and the impact on radar-variable estimates is comparable to that obtained when operating the same system as a stationary PAR. That is, by using MCS and compensating for antenna motion, the radar matches the performance of a stationary PAR system. Nevertheless, intrinsic scan-dependent measurement biases coming from the copolar antenna patterns (present in both the stationary PAR and MCS-RPAR, as shown in Fig. 8) must be addressed.

It is understood that stationary PAR systems are subject to scan-dependent measurement biases coming from the antenna patterns as they are electronically steered in various directions [34]. These are caused by the H and V copolar antenna patterns that vary with beam steering direction and are quantified on the first column of Fig. 8 for the ATD system when it is operated as a stationary PAR system. The effects of these variations can be addressed via corrections using appropriate values at each broadside location. If the cross-coupling effects are sufficiently suppressed with phase coding [35] and given a sufficiently narrow antenna main beam, the corrections can be conducted using only the measurements of the copolar pattern peaks [36]. Considering that biases in the stationary PAR and the RPAR using MCS are comparable, radar-variable corrections for the copolar biases of the ATD operated as a stationary system derived by [37], [38] are used to demonstrate the RPAR using MCS in Section IV.

IV. Practical Implementation and Demonstration of MCS on the ATD

The recently installed ATD radar system at the NSSL in Norman, OK, is an active S-band planar dual-polarization PAR. It was funded jointly by NOAA and the Federal Aviation Administration (FAA). It is being developed by the NSSL, the Cooperative Institute for Mesoscale Meteorological Studies (CIMMS) at the University of Oklahoma, MIT Lincoln Laboratory, and General Dynamics Mission Systems [39]. The main purpose of this proof-of-concept system is to evaluate the suitability of PAR technology for weather observations, but it was not designed to meet the beamwidth or sidelobe-level requirements specified in [4]. For a stationary PAR system designed to meet the beamwidth and sidelobe-level requirements, using MCS when operating this system as an RPAR would mitigate beam smearing without increasing the sidelobe levels (since MCS steering angles are small). That is, the system would still meet the requirements when using MCS, because the sidelobe structure of the effective MCS pattern is approximately the same as that of the stationary PAR. The beam steering generator allows pulse-to-pulse control of the steering angle for transmitted H and V signals, which makes this system capable of implementing both MCS CONOPS presented here.

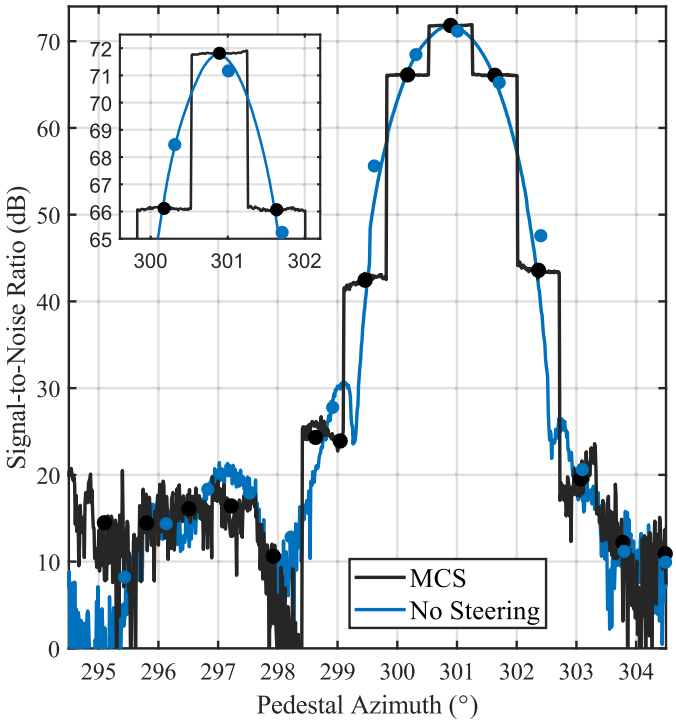

Fig. 10. SNR of signals received by the ATD system on the H polarization while rotating past the target as a function of the pedestal (i.e., mechanical) azimuth. Solid lines show the single-pulse SNR and dot markers show the SNRs estimated by averaging those from the M samples in each CPI.

The BMCS and FB-MCS CONOPS were implemented on the ATD to demonstrate these concepts in an experimental research environment. First, a point target was scanned with BMCS to validate the practical implementation and to quantify the beam pointing offset. Then, both BMCS and FB-MCS were used to illustrate the MCS technique for polarimetric weather observations. The FB-MCS was implemented with the parameters defined in Table I.

A. Point-Target Experiment

Successful implementation and calibration of the MCS technique were verified by rotating the antenna while scanning past a stationary point target located in the vicinity of the ATD. Specifically, a set of data were collected with the ATD rotating over a ∼20° sector at $\omega = 4\ ^\circ\ \mathrm{s}^{-1}$, $M = 65$, and $T_s = 3$ ms. The antenna broadside was commanded to rotate from 290° to 310° azimuth with respect to North, with the target located at 31.65 km in range and approximately 300.96° azimuth with respect to North. The antenna broadside was positioned to a 0.5° mechanical elevation. Two subsequent scans were conducted: 1) the transmit and receive beams were electronically maintained at broadside in azimuth and elevation and 2) the transmit and receive beams were electronically steered in azimuth and elevation using the BMCS CONOPS in Section II-C1. The pointing angles for 2) were initially obtained using the theoretical expression (20), but were not sufficiently accurate as the pedestal positioner is not able to maintain a perfectly constant rotation speed. A model of the ATD's mechanical motion in azimuth was derived by fitting third-order polynomials to pedestal positions measured at a rate of 10 Hz when the system was commanded to rotate at the speeds of 2, 4, and 8° s^{-1}. This model agreed well with the theoretical expression in (20) for the linear and constant terms

$$\tilde{\phi}^{A}_{\mathrm{BMCS}}(mT_s) = 0.0034(mT_s)^3 + \cdots \\ \cdots + 0.052(mT_s)^2 + \omega T_s\left[\frac{(M-1)}{2} - m\right] \quad (21)$$

and was adopted for the practical implementation of MCS on the ATD under both CONOPS presented as the pedestal motion is independent of electronic steering angle.

The SNR of signals received by the ATD on the H polarization while rotating past the target as a function of the pedestal (i.e., mechanical) azimuth is presented in Fig. 10. The platform's mechanical azimuth (with respect to North) is used to compare the SNRs measured with MCS with those from a mechanically scanning antenna (i.e., not using MCS). Solid lines show the single-pulse SNR estimates and dot markers show the SNRs estimated by averaging those from the M samples in each CPI (herein referred to as the CPI estimate). The blue line represents the SNRs for the RPAR not using MCS and its shape resembles the mainlobe of the two-way antenna patterns. The solid black line represents the single-pulse SNRs of the RPAR using MCS and its shape resembles a staircase plot where the SNRs at each step are sampling approximately the same resolution volume, and therefore the returned powers are approximately constant. The inset plot shows that the CPI estimate obtained using MCS is 71.81 dB while that obtained without MCS is 71.16 dB. It is apparent that CPI estimates obtained using MCS are closer to true SNRs, since estimates are closer to the single-pulse SNRs on the blue curve, in particular, the peak SNR return from

TABLE II
RADAR SYSTEM PARAMETERS AND SCAN STRATEGIES

Scan #	Radar System	Time (Z)	Electronic Steering	Scanned Sector	Mechanical Elevation	ϕ_l	ϕ_e	M	T_s (ms)	ω (m s^{-1})
1	ATD	00:44:25	No	130° - 170°	0.9°	1.58°	1.74°	65	3	4
2	ATD	00:44:47	BMCS	130° - 170°	0.9°	1.58°	1.58°	65	3	4
3	KCRI	00:44:36	No	0° - 360°	0.9°	1°	1.12°	15	3	21.15

the point target which is 71.82 dB. Furthermore, the standard deviation of single-pulse SNRs for the samples in the CPI that contains the peak return (∼301°) is 0.033 dB with MCS, and 0.61 dB without MCS. This order of magnitude reduction in the variance of SNRs from a point target indicates that power estimate biases arising from approximately concentric nonuniform resolution volumes are much smaller than those from nonconcentric uniform volumes.

The mean standard deviation of absolute azimuth pointing angles (i.e., the summation of the mechanical and electronic azimuths) of samples within CPIs is 0.008° with MCS, and 0.21° without MCS. This average standard deviation of pointing angles measured when using MCS is used to characterize the pointing offset, which is consistent with that obtained in the simulations presented in Section III (∼0.006°). The small difference between simulated and measured standard deviation of pointing angles is largely due to mechanical system imperfections, which were not considered in the simulations. Using $\varepsilon \leq \pm 0.085$ (for $\chi = 0.99$), and (17) with $\phi_{1h} = 1.58°$, a pointing offset of $\Delta_\phi \leq \pm 0.143°$ is obtained for the ATD system. Since this pointing offset is much larger than the measured standard deviation of MCS pointing angles, the performance is considered acceptable to largely mitigate beam smearing using the ATD system without impacting polarimetric data quality.

B. Polarimetric Weather Observations

1) BMCS CONOPS: The first experiment is used to illustrate the BMCS CONOPS whereby MCS is used to compensate the radar motion for samples within a CPI centered on the elevation principal plane. Sector scans were collected in rapid succession using the STSR mode on May 5, 2020 to sample a rapidly evolving mesoscale convective system at a range of approximately 100 km. For scan 1, the ATD rotated at $\omega = 4° \text{ s}^{-1}$, the transmit and receive pencil beams were maintained at broadside ($\phi_{az} = 0°$, $\theta_{el} = 0°$), mimicking the operation of a conventional reflector-based radar. Data from this scan were collected at 00:44:25 Z, and are used here to verify the BMCS data. For scan 2, the ATD rotated at $\omega = 4° \text{ s}^{-1}$, the transmit and receive pencil beams were collected using BMCS. Data from this scan were collected 22 s after scan 1, at 00:44:47 Z. For these scans, the radar broadside was commanded to mechanically rotate clockwise from 130° to 170° in azimuth, at constant 0.9° elevation, with a continuous pulse transmission at $T_s = 3$ ms. For a normalized azimuthal sampling of $\Delta\phi = 0.5$, the number of samples M was set to 65 on both scans. Receiver range-time samples were produced at a rate of 4 MHz, which results in a range sampling interval of 37.5 m. Range-time processing was set to incoherently average samples from six consecutive range gates, which results in a range sampling spacing for the radar variables of 225 m.

Data produced with this technique were verified by comparing them to data from a WSR-88D radar system, that has an inherently better angular resolution than the ATD. The KCRI radar in Norman, OK is operated and maintained by the Radar Operations Center and it is collocated with the ATD. The KCRI radar was following the operational VCP number 212, which commands the antenna system to rotate at 21.15° s^{-1} at the 0.9° elevation angle. For this elevation, the CPIs from the surveillance scan consist of 15 samples at $T_s = 3$ ms, with $\Delta\phi = 1$ (i.e., azimuthal sampling of 1° since the HPBW of this system is approximately 1°), and a $\phi_e \sim 1.12°$. Super-resolution processing is used in the WSR-88D, whereby the azimuthal spacing of CPIs is 0.5°. Data for the lowest elevation of the VCP were collected with the KCRI radar at 00:44:36 Z, and IQ data from the same azimuthal sector were extracted for processing. There are several architectural differences between the ATD and KCRI systems, but since the KCRI has better effective angular resolution it is considered here as a reference to verify the angular resolution enhancement of the MCS technique. Radar system parameters and scan strategies for these experiments are summarized in Table II.

Fields of radar-variable estimates resulting from processing the data from these scans are presented in Fig. 11. Panels are organized as follows: the top row corresponds to scan 1, the middle row corresponds to scan 2, and the bottom row corresponds to scan 3; the columns from left to right show fields of radar Z_h, Z_{DR}, differential phase (Φ_{DP}), and ρ_{hv}. Qualitative comparison of radar-variable estimates from scans 1 and 2 shows there are no apparent artifacts in the data from scan 2 (MCS), and both data sets appear to have similar meteorological features as that of scan 3. Data from scans 1 and 2 have a smoother texture than data from scan 3, likely due to the higher number of samples, which results in the reduced standard deviation of radar-variable estimates. Regions with well-defined meteorological features are highlighted with black arrows for discussion. Comparing the highlighted regions on fields of Z_h, it is apparent that the line of high Z_h (>50 dBZ) presents a finer structure in the field estimated with MCS data. This is also apparent in other areas on fields of Z_h, consistent with the hypothesis that MCS reduces beam smearing. Similar conclusions are drawn from

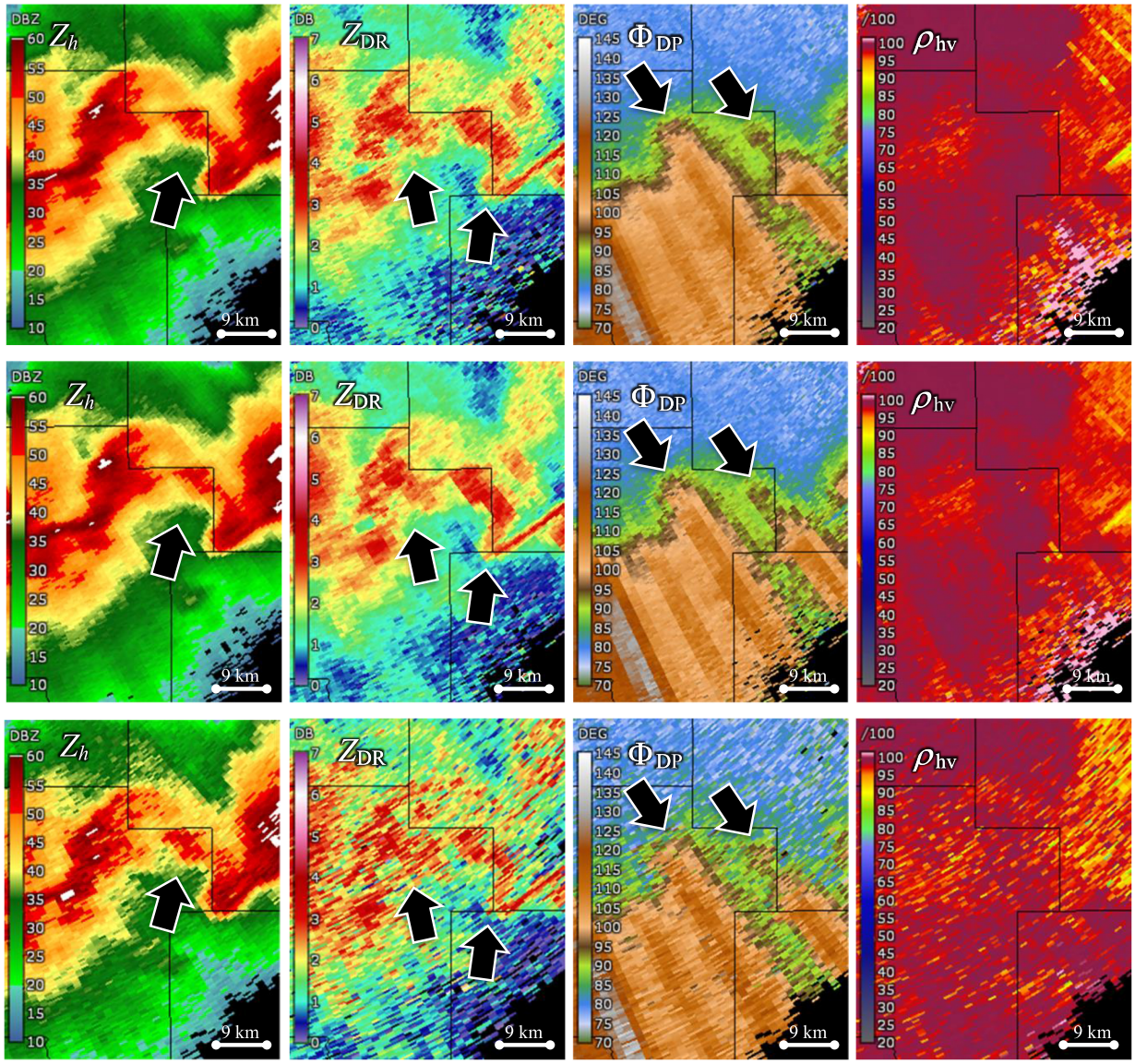

Fig. 11. Radar-variable estimates were obtained from three scans collected in rapid succession. Panels are organized as follows. (Top row) Scan 1 (ATD—No MCS). Scan 2 (ATD BMCS). (Bottom row) Scan 3 (KCRI—No MCS). The columns from left to right show fields of Z_h, Z_{DR}, Φ_{DP}, and ρ_{hv}, respectively.

a qualitative comparison of fields of Z_{DR} (specially in regions highlighted with black arrows). Comparing the fields of Φ_{DP} from scans 1 and 2 in this region, it is apparent that scan 2 exhibits a narrower and more defined line with increasing values of Φ_{DP} along the beams with high Z_h (see black arrows in fields of Φ_{DP}). Since Φ_{DP} represents the difference in phase from the H and V polarizations along the wave propagation path, it typically presents radially oriented features. In this case, it is apparent that the high radially oriented Z_h core attenuates the vertically polarized waves, which results in the increase of Φ_{DP}. The narrower appearance of this feature in the field of Φ_{DP} from scan 2 (i.e., BMCS) resembles that of scan 3. Comparing the fields of ρ_{hv} from scans 1 and 2 in this region, it is observed that scan 2 exhibits generally higher values (i.e., closer to 1). Considering that the time difference between these scans is relatively short (∼22 s) and that the same noise-power estimation technique is used for all three scans [38], the improvement in ρ_{hv} estimates is attributed to the use of MCS.

To quantify the differences in the fields of radar-variable estimates produced by scans 1 and 2, the absolute difference of each of these with scan 3 is calculated. Since data from scan 3 inherently have better azimuthal resolution, data from scans 1 and 2 are compared to it by using the absolute difference of estimates. Note that the effective beamwidth of the ATD for scans 1 and 2 is 1.74° and 1.58°, as indicated in Table II. Given that sampling grids are different, a simple nearest neighbor interpolation is used to map the data from scans 1 and 2 on the sampling grid of scan 3. The notation $|\delta x|$ is used, where x is one of the radar variables presented in Fig. 11. An SNR threshold of 8 dB is used to censor data corresponding to weak returns (painted in gray for reference). Further, to reduce the variance of differences, a running average of five gates in the range

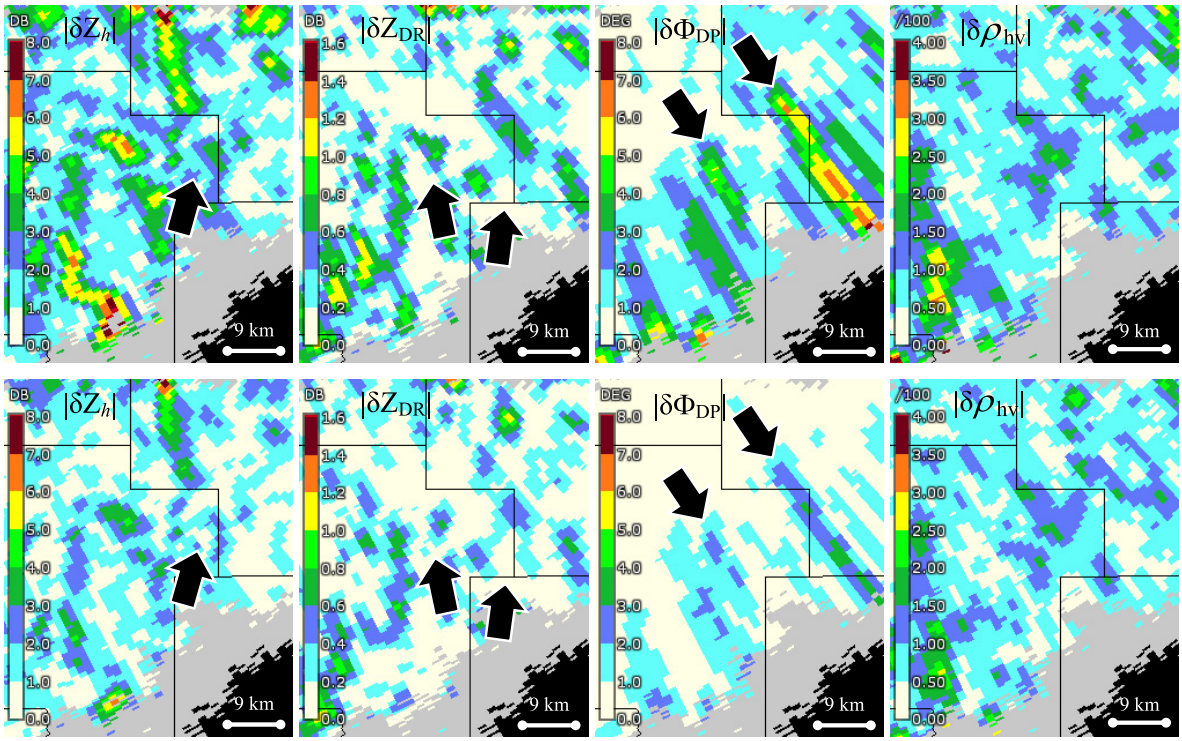

Fig. 12. Absolute differences between fields of radar-variable estimates in Fig.11. (Top row) Absolute differences between scans 1 and 3. (Bottom row) Absolute differences between scans 1 and 2. Columns from left to right show absolute difference fields of Z_h, Z_{DR}, Φ_{DP}, and ρ_{hv}, respectively.

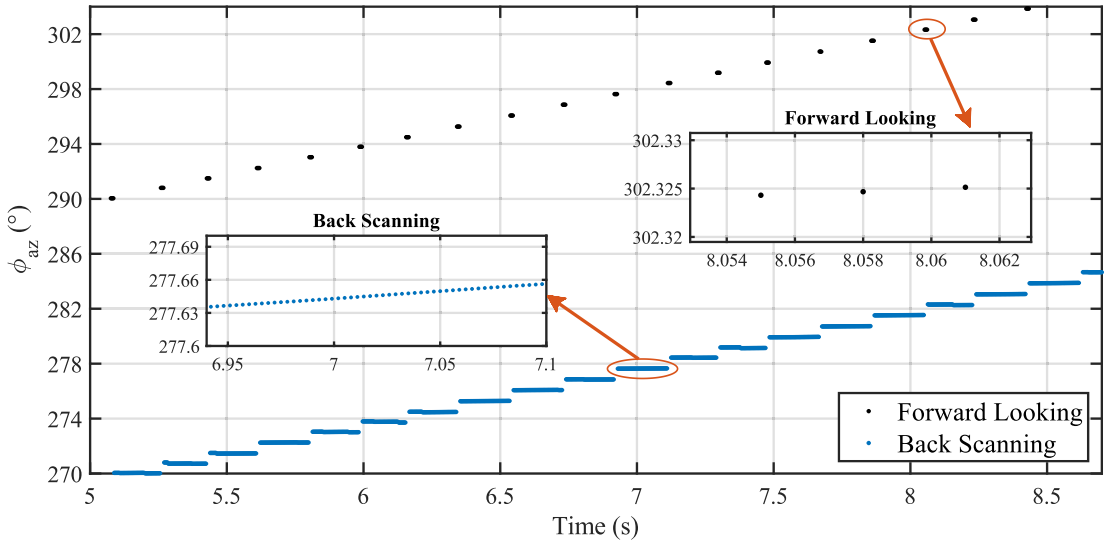

Fig. 13. Azimuth angles of a subset of pulses in scan 2 as a function of time. These illustrate the scan angles of the FB-MCS CONOPS.

is applied on the direct absolute differences (no averaging in azimuth is applied to preserve resolution). Results are presented in Fig. 12, where the top row represents the absolute differences between scans 1 and 3, and the bottom row represents absolute differences between scans 2 and 3. Black arrows are used to highlight regions corresponding to those discussed in Fig. 11. Fields of $|\delta Z_h|$, $|\delta Z_{DR}|$ and $|\delta \Phi_{DP}|$ reveal considerable improvement, i.e., lower absolute differences in estimated fields with respect to the KCRI estimates. For the $|\delta Z_h|$ fields, there is a reduction from ∼3–4 dB (scan 1) to ∼1–2 dB (scan 2) in the highlighted region. For the $|\delta Z_{DR}|$ fields, there is a reduction from ∼0.6–0.8 dB (scan 1) to ∼0.4–0.6 dB (scan 2) in the highlighted region. For the $|\delta \Phi_{DP}|$ fields, there is a reduction from ∼4°–7° (scan 1) to ∼1°–3° (scan 2) in the highlighted regions. As noted when comparing fields of ρ_{hv} estimates, there appears to be no significant differences in the field $|\delta \rho_{hv}|$. These biases are relatively large (whether MCS is used or not); this is a consequence of the significant difference in the intrinsic beamwidths of the ATD and KCRI radars. Since the CPIs of the ATD scans are identical and estimates from both are compared to estimates from the scan of the collocated KCRI radar (with a time difference of only 22 s), differences observed are mostly a consequence of the different azimuthal resolution.

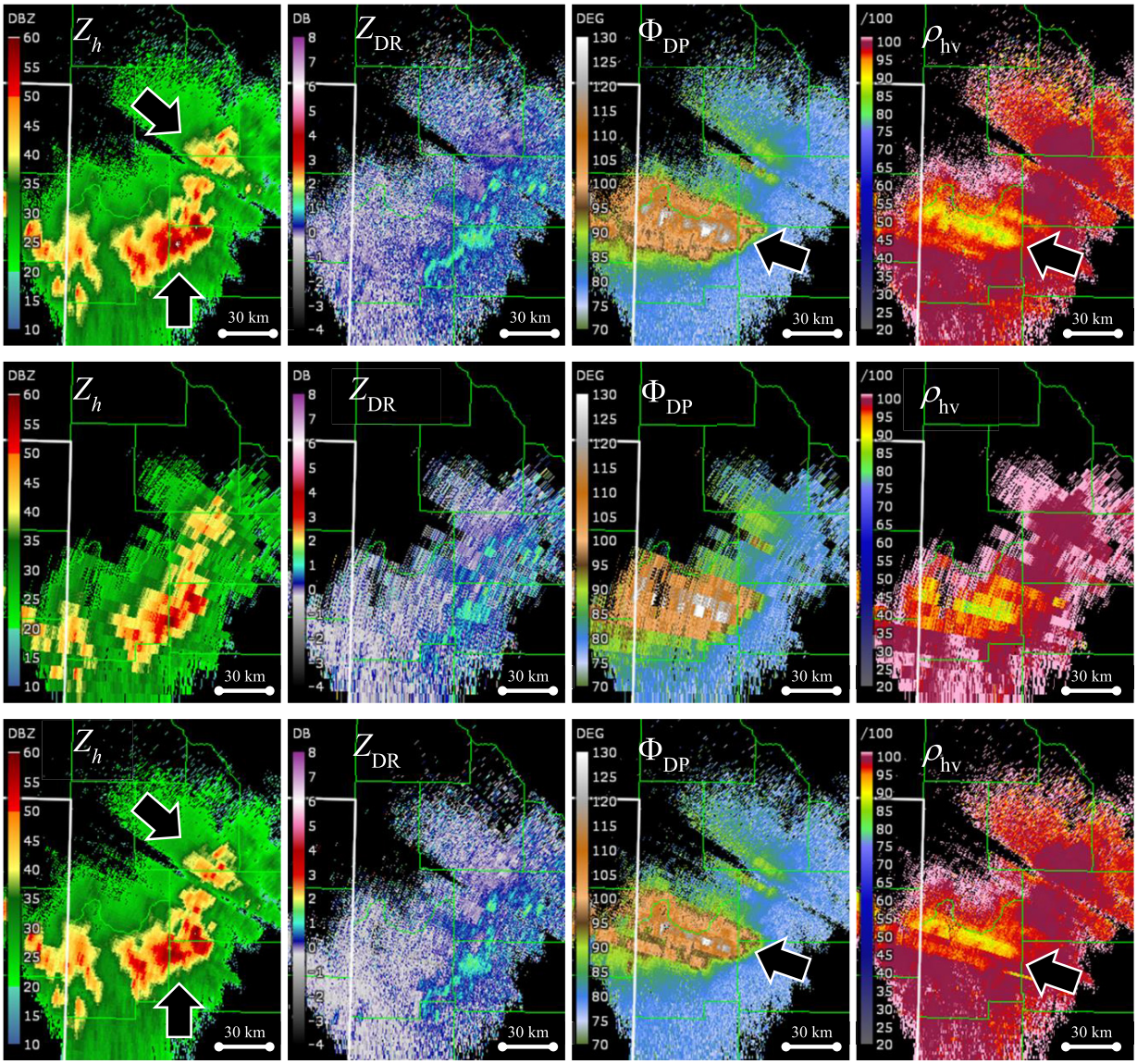

Fig. 14. Radar-variable estimates obtained from two scans collected in rapid succession. Panels are organized as follows. (Top row) Scan 1 (ATD—No MCS), (Middle row) Forward-looking beams of scan 2 (ATD FB-MCS). (Bottom row) Back-scanning beams of scan 2 (ATD FB-MCS). The columns from left to right show fields of Z_h, Z_{DR}, Φ_{DP}, and ρ_{hv}, respectively.

Results presented show that data produced using the BMCS CONOP have better azimuthal resolution than that obtained with no beam steering. Furthermore, no apparent data artifacts were observed in the polarimetric estimates obtained using MCS, which is consistent with the conclusions from Section III-B.

2) FB-MCS CONOPS: The second experiment is used to illustrate the FB-MCS CONOPS whereby MCS is used to compensate the radar motion for samples within a CPI at steering angles away from the broadside. Two sector scans were collected using the STSR mode in rapid succession on June 4, 2020 to sample a convective precipitation system approaching the ATD from the West, at a range of approximately 150 km. For scan 1, the radar rotated at $\omega = 4^\circ$ s^{-1}, the transmit and receive pencil beams were maintained at broadside ($\phi_{az} = 0^\circ$, $\theta_{el} = 0^\circ$), mimicking the operation of a conventional reflector-based radar. Data from this scan were collected at 23:17:40 Z. The number of samples was M set to 65 for a normalized azimuthal sampling of $\Delta\phi = 0.5$ at $T_s = 3$ ms. For scan 2, the ATD rotated at $\omega = 8^\circ$ s^{-1}, the transmit and receive beams were collected using FB-MCS. A set of 5 simultaneous forward-looking beams were collected with $M_F = 3$ at $T_{sF} = 3$ ms, using a transmit beam spoiled by a factor of 3, and a $\Delta\phi = 1$. The back-scanning beams were collected with $M_B = 61$ at $T_{sB} = 1.48$ ms. The normalized azimuthal sampling for the back-scanning beams is $\Delta\phi = \omega(T_{sF}M_F + T_{sB}M_B)/\phi_1(10^\circ) = 0.5$. Notice that the azimuthal sampling spacings for the FB beams can be set arbitrarily and may be different. Data from scan 2 were collected 33 s after scan 1, at 23:18:13 Z. For both scans, the radar broadside was commanded to mechanically rotate clockwise from 250° to 330° in azimuth, at constant 0.5° elevation. The range sampling was the same as in the previous experiment.

Azimuth angles of a subset of pulses in scan 2 are shown in Fig. 13 as a function of time to illustrate the CONOPS. Dot markers in blue represent the back-scanning beams and dot markers in black represent the forward-looking beams. Notice that FB beams are interleaved, and azimuth angles for pulses within a CPI appear to be approximately constant. Inset plots provide close-up views of samples within a CPI for each type of beam. For the selected forward-looking CPI, the span of azimuth angles is 0.0008°, and for the selected back-scanning CPI the span of azimuth angles is 0.024°. The larger spread on the latter one is a consequence of the higher number of samples and a small slope ($\sim 0.12^\circ\ s^{-1}$, due to variability in the mechanical motion but considered negligible for the purposes of this work).

Fields of radar-variable estimates resulting from processing the data from these scans are presented in Fig. 14. Panels are organized as follows: the top row corresponds to scan 1, the middle row corresponds to the forward-looking beams in scan 2, and the bottom row corresponds to the back-scanning beams in scan 2; the columns from left to right show fields of Z_h, Z_{DR}, Φ_{DP}, and ρ_{hv}. Distributed Beams (DB) technique [40], [41] was used to exploit the simultaneously received beams in azimuth and to produce data from the forward-looking beams with reduced variance. Qualitative comparison of radar-variable fields shows no apparent data artifacts from either scan. Qualitative comparison of the fields derived from scan 1 (top row) and those derived from the back-scanning beams in scan 2 (bottom row) shows features that appear to be narrower in the data from scan 2 in the region highlighted by the black arrows. Note that polarimetric-variable estimates for the forward-looking ($\phi_p = +10^\circ$) and back-scanning ($\phi_p = -10^\circ$) beams were corrected using the methods described in [37]. In contrast to fields from the back-scanning beams on scan 2, the forward-looking beams have reduced angular resolution and sensitivity. This was intended since the forward-looking beams were designed to provide sufficient information of upcoming meteorological regions of interest (ahead of the radar motion).

Three key takeaways are derived from these results. First, Fig. 13 shows that an implementation of the FB-CONOPS with sufficient beam pointing accuracy for MCS is achievable on the ATD system. Second, results presented in Fig. 14 show that it is possible to implement MCS at steering angles away from the broadside, and to produce calibrated radar-variable estimates without apparent radar sampling artifacts caused by MCS. Lastly, it illustrates that data from the forward-looking beams have sufficient meteorological information and could be used by an adaptive algorithm to improve the quality of estimates. As described earlier, information from forward-looking beams could be used to: 1) decide if there are significant weather echoes in upcoming beam positions and 2) determine the maximum range of storms observed and shorten the PRTs of back-scanning beams to match the unambiguous range with that of the maximum range of observed storms (increasing the Nyquist co-interval). We emphasize that the introduction of the FB-CONOPS serves to motivate the use of MCS at off-broadside angles (in contrast to the BMCS CONOPS), which could be beneficial for other applications. Future research efforts could implement this CONOPS with a real-time scheduler to adaptively scan the back-scanning beams with tailored dwell times to improve the quality of estimates using an RPAR.

V. Summary

The demanding *Optimal Functional Requirements* developed by the NWS for a future weather surveillance radar will likely require exploiting advanced radar capabilities. The RPAR architecture may be an affordable candidate system that could meet requirements when operated under certain CONOPS. In particular, the ambitious angular resolution requirements could drive the cost of the antenna system, which has to be sufficiently large to produce an effective beamwidth that meets mission needs. Further investigation of techniques that exploit PAR's unique capabilities in the context of an RPAR CONOPS has to be done.

By exploiting a PAR's unique dynamic capabilities in conjunction with the application of advanced signal processing techniques, we demonstrated that it is possible to design an RPAR CONOPS capable of enhancing the angular resolution of the system. That is, by electronically steering the beam on a pulse-to-pulse basis within the CPI, the motion of the antenna can be compensated to maintain the beam pointed at the center of resolution volume being sampled. This MCS can reduce the apparent motion of the antenna and lead to a reduction in the effective beamwidth. In turn, mitigating the impact of beam smearing allows for smaller (and more affordable) antenna apertures that can meet effective-beamwidth requirements, which could translate into a simpler and less costly radar system.

The MCS technique was introduced and expressions for the MCS pointing angles were provided for the general case with the antenna plane tilted with respect to earth. A theoretical analysis of the impact of MCS on the quality of signal power and copolar correlation coefficient estimates was done to derive simple expressions that provide the upper bound for beam pointing offset to achieve the required bias in correlation coefficient estimates. Two alternative CONOPS were introduced and discussed: the BMCS and the FB-MCS. The BMCS CONOPS produces sampling of concentric nonuniform resolution volumes centered around the elevation principal plane, while the FB-MCS CONOPS produces sampling of concentric nonuniform resolution volumes at arbitrary angles off the broadside (within the visible region). The proposed FB-MCS CONOPS, whereby forward-looking beams are used to inform the back-scanning beams in the scan, is intended for use in an adaptive scanning context.

Through high fidelity RPAR simulations, we quantified the effectiveness of MCS in mitigating beam smearing as a function of antenna phase shifter bits, antenna size, and normalized azimuthal sampling. It was demonstrated that for relatively large planar RPARs, 6-bit phase shifters provide sufficient pointing accuracy to effectively implement MCS and mostly mitigate beam smearing, while 7-bit phase-shifters would be desirable to largely eliminate smearing effects.

The cost of phase shifters is approximately proportional[4] to the number of bits required for steering resolution. Several factors can affect their cost (e.g., market volume, material technology), which can be considered relatively small with respect to other components in the phased array antenna (i.e., element-level power amplifiers). Therefore, increasing the number of bits for more accurate steering resolution would not be a major cost driver, and is recommended to use 7-bits of resolution to mitigate beam smearing with the MCS technique presented in this article. Further, the impacts of copolar beam steering biases resulting from the use of MCS were quantified over a large scan sector using simulations and were found to be negligible with respect to the stationary operation of the same PAR. These simulations were tailored for the architecture of the polarimetric ATD radar system in Norman, OK. The BMCS and FB-MCS CONOPS were implemented on the ATD system to demonstrate the MCS technique. First, a point target located in the vicinity of the ATD system was scanned without electronic beam steering (i.e., mimicking a parabolic-reflector antenna) and with BMCS. It was shown that the BMCS implementation on the ATD provides sufficient pointing accuracy to mitigate beam-smearing effects. Both CONOPS introduced were demonstrated by scanning meteorological scatterers. Fields of polarimetric-variable estimates from the BMCS CONOPS were compared to those obtained when scanning without beam steering. These results were verified by quantifying absolute radar-variable-estimate differences with respect to a WSR-88D system (KCRI) that has inherently better azimuthal resolution. The BMCS data were shown to produce fields of radar-variable estimates with generally narrower features (more apparent in reflectivity and differential phase). Finally, the FB-MCS CONOPS was illustrated by scanning meteorological scatterers and qualitatively comparing fields of radar-variable estimates from the FB beams to those obtained when scanning without beam steering.

In summary, we demonstrated that the MCS technique is capable of enhancing the azimuthal resolution of the RPAR and could be used for several polarimetric weather radar applications. Furthermore, the technique could be integrated with other advanced complementary techniques to attain the performance levels required to meet all radar functional requirements. For example, in conjunction with MCS, advanced beamforming techniques could be used to reduce the scan update times by receiving multiple simultaneous beams (in azimuth and/or elevation). If the pointing accuracy of antenna elements is insufficient, the RPAR is unable to accurately sample concentric resolution volumes using MCS. That is, the performance of MCS in mitigating beam smearing may be limited if the beam cannot be pointed with sufficient accuracy. This could be caused by either the accuracy of electronic beam steering (i.e., the number of phase shifter bits and the element phase noise) or the precision of the mechanical rotator. While increasing the number of bits per antenna element may increase system cost, it is likely that increasing the antenna aperture (i.e., for an equivalent effective beamwidth) would be more costly. Furthermore, MCS may not be compatible with other advanced PAR scanning techniques (e.g., adaptive beamforming), which may limit the capabilities of the overall system. The architectural analysis involving the size of the aperture and the cost of antenna elements is beyond the scope of this work.

Future plans for the RPAR CONOPS include a thorough evaluation of the integration of the MCS technique with the DB technique, whereby multiple simultaneously received beams can be coherently combined and processed to reduce the scan update time and/or the variance of radar-variable estimates. This would exploit the PAR's beam agility to enhance the CONOPS and allow for both a scan time reduction while maintaining data quality and angular resolution (of the stationary PAR). In turn, it could eliminate the need for split-cuts (such as those used in the VCPs of WSR-88Ds), whereby the same elevation angle is scanned twice with different PRTs as a means to mitigate range-and-velocity ambiguities. It is expected that the outcome of these research efforts will continue to provide valuable information that can support the next design of the future U.S. weather surveillance radar network.

APPENDIX A

To account for antenna tilt on the calculation of MCS steering angles, it is first noted that each location ϕ, θ, r in spherical coordinates can be expressed in the Cartesian system as

$$\begin{aligned} x &= r\sin\theta\cos\phi \\ y &= r\sin\theta\sin\phi \\ z &= r\cos\theta. \end{aligned} \tag{22}$$

If the antenna is tilted by θ_T, each location with coordinates $(x,\ y,\ z)$ in the Cartesian coordinate system referenced to the ground has the corresponding location $(x_A,\ y_A,\ z_A)$ in the Cartesian system referenced to the antenna. Given ϕ, θ, r, the location $(x_A,\ y_A,\ z_A)$ can be found using the rotation matrix as

$$\begin{aligned} \begin{bmatrix} x_A \\ y_A \\ z_A \end{bmatrix} &= \begin{bmatrix} \cos\theta_T & 0 & \sin\theta_T \\ 0 & 1 & 0 \\ -\sin\theta_T & 0 & \cos\theta_T \end{bmatrix} \begin{bmatrix} x \\ y \\ z \end{bmatrix} \\ &= \begin{bmatrix} r\sin\theta\cos\phi\cos\theta_T + r\cos\theta\sin\theta_T \\ r\sin\theta\sin\phi \\ -r\sin\theta\cos\phi\sin\theta_T + r\cos\theta\cos\theta_T \end{bmatrix}. \end{aligned} \tag{23}$$

Then, each location ϕ, θ in spherical coordinates tied to the ground has the corresponding location ϕ^A, θ^A in spherical coordinates referenced to the antenna as

$$\begin{aligned} \phi^A &= \arctan\left(\frac{y_A}{x_A}\right) \\ &= \arctan\left(\frac{\sin\theta\sin\phi}{\sin\theta\cos\phi\cos\theta_T + \cos\theta\sin\theta_T}\right). \\ \theta^A &= \arccos\left(\frac{z_A}{\sqrt{x_A^2 + y_A^2 + z_A^2}}\right) \\ &= \arccos(-\sin\theta\cos\phi\sin\theta_T + \cos\theta\cos\theta_T). \end{aligned} \tag{24}$$

[4]Approximate phase-shifter costs were obtained for S-band phase shifters (2.3–3.8 GHz) assuming tens of thousands of units are ordered, and were approximately U.S. $20, U.S. $40, and U.S. $60 for 5, 6, and 7 bits of steering resolution.

Thus, if desired scan angle is at ϕ_0, θ_0 (in the spherical coordinates referenced to the ground) the commanded location to which the tilted array must steer the beam, to point at ϕ_0, θ_0, is found using (24). Following the same rationale, each location ϕ^A, θ^A in spherical coordinates referenced to the antenna has the corresponding location ϕ, θ in spherical coordinates tied to the ground as

$$\phi = \arctan\left(\frac{\sin\theta^A \sin\phi^A}{\sin\theta^A \cos\phi^A \cos\theta_T^A - \cos\theta^A \sin\theta_T}\right)$$
$$\theta = \arccos\left(\sin\theta^A \cos\phi^A \sin\theta_T + \cos\theta_A \cos\theta_T\right). \quad (25)$$

ACKNOWLEDGMENT

The authors would like to extend their gratitude to Dušan Zrnić (NOAA-NSSL), Henry Thomas (MIT-LL), Antone Kusmanoff (OU JHLP), and Feng Nai (OU-CIMMS), Alexander Morris (MIT-LL), and anonymous reviewers for the useful discussions and comments that improved this article. They thank Igor Ivić (OU-CIMMS) for providing tools to simulate PAR antenna patterns. They would like to extend our appreciation to the entire ATD team. Special thanks go to Christopher Schwarz (OU-CIMMS), Daniel Wasielewski (NOAA-NSSL), Rafael Mendoza (NOAA-NSSL), and John "Chip" Murdock (GD-MS), for their support configuring and operating the ATD. They would also like to acknowledge the contributions of numerous engineers, students, scientists, and administrators who have supported the research and development of Phased Array Radar technology for weather observations over the last decade.

REFERENCES

[1] D. S. Zrnic and A. V. Ryzhkov, "Polarimetry for weather surveillance radars," *Bull. Amer. Meteorolog. Soc.*, vol. 80, pp. 389–406, Mar. 1999, doi: 10.1175/1520-0477(1999)080<0389:PFWSR>2.0.CO;2.

[2] K. A. Scharfenberg *et al.*, "The joint polarization experiment: Polarimetric radar in forecasting and warning decision making," *Weather Forecasting*, vol. 20, no. 5, pp. 775–788, Oct. 2005, doi: 10.1175/WAF881.1.

[3] K. Hondl and M. Weber, "NOAA's meteorological phased array radar research program," in *Proc. IEEE Int. Symp. Phased Array Syst. Technol. (PAST)*, Oct. 2019, pp. 1–6, doi: 10.1109/PAST43306.2019.9020994.

[4] NOAA/NWS. (2015). *Radar Functional Requirements*. [Online]. Available: https://roc.noaa.gov/WSR88D/PublicDocs/NOAA_Radar_Functional_Requirements_Final_Sept%202015.pdf

[5] D. S. Zrnic and R. J. Doviak, "Effective antenna pattern of scanning radars," *IEEE Trans. Aerosp. Electron. Syst.*, vol. AES-12, no. 5, pp. 551–555, Sep. 1976, doi: 10.1109/TAES.1976.308254.

[6] R. Doviak and D. S. Zrnic, *Doppler Radar and Weather Observations*. Mineola, NY, USA: Dover, 2006.

[7] R. A. Brown, L. R. Lemon, and D. W. Burgess, "Tornado detection by pulsed Doppler radar," *Monthly Weather Rev.*, vol. 106, pp. 29–38, Jan. 1978, doi: 10.1175/1520-0493(1978)106<0029:TDBPDR>2.0.CO;2.

[8] R. A. Brown, V. T. Wood, and D. Sirmans, "Improved tornado detection using simulated and actual WSR-88D data with enhanced resolution," *J. Atmos. Ocean. Technol.*, vol. 19, pp. 1759–1771, Nov. 2002, doi: 10.1175/1520-0426(2002)019<1759:ITDUSA>2.0.CO;2.

[9] National Research Council, *Weather Radar Technology Beyond NEXRAD*. Washington, DC, USA: National Academies Press, 2002.

[10] T.-Y. Yu, M. B. Orescanin, C. D. Curtis, D. S. Zrnić, and D. E. Forsyth, "Beam multiplexing using the phased-array weather radar," *J. Atmos. Ocean. Technol.*, vol. 24, no. 4, pp. 616–626, Apr. 2007, doi: 10.1175/JTECH2052.1.

[11] P. L. Heinselman, D. L. Priegnitz, K. L. Manross, T. M. Smith, and R. W. Adams, "Rapid sampling of severe storms by the national weather radar testbed phased array radar," *Weather Forecasting*, vol. 23, no. 5, pp. 808–824, Oct. 2008, doi: 10.1175/2008WAF2007071.1.

[12] S. M. Torres *et al.*, "Adaptive-weather-surveillance and multifunction capabilities of the national weather radar testbed phased array radar," *Proc. IEEE*, vol. 104, no. 3, pp. 660–672, Mar. 2016, doi: 10.1109/JPROC.2015.2484288.

[13] J. Herd *et al.*, "Multifunction phased array radar (MPAR) for aircraft and weather surveillance," in *Proc. IEEE Radar Conf.*, May 2010, pp. 945–948, doi: 10.1109/RADAR.2010.5494483.

[14] J. E. Stailey and K. D. Hondl, "Multifunction phased array radar for aircraft and weather surveillance," *Proc. IEEE*, vol. 104, no. 3, pp. 649–659, Mar. 2016, doi: 10.1109/JPROC.2015.2491179.

[15] D. S. Zrnic *et al.*, "Agile-beam phased array radar for weather observations," *Bull. Amer. Meteorolog. Soc.*, vol. 88, no. 11, pp. 1753–1766, Nov. 2007, doi: 10.1175/BAMS-88-11-1753.

[16] R. J. Mailloux, *Phased Array Antenna Handbook*. Norwood, MA, USA: Artech House, 2017.

[17] R. A. Brown and V. T. Wood, "Simulated vortex detection using a four-face phased-array Doppler radar," *Weather Forecasting*, vol. 27, no. 6, pp. 1598–1603, Dec. 2012, doi: 10.1175/WAF-D-12-00059.1.

[18] M. E. Weber, "Meteorological phased array radar research at NOAA's national severe storms laboratory," in *Proc. IEEE Int. Conf. Microw., Antennas, Commun. Electron. Syst. (COMCAS)*, Nov. 2019, pp. 1–6, doi: 10.1109/COMCAS44984.2019.8958067.

[19] J. C. Kirk, "Motion compensation for synthetic aperture radar," *IEEE Trans. Aerosp. Electron. Syst.*, vol. AES-11, no. 3, pp. 338–348, May 1975, doi: 10.1109/TAES.1975.308083.

[20] D. C. Law *et al.*, "An electronically stabilized phased array system for shipborne atmospheric wind profiling," *J. Atmos. Ocean. Technol.*, vol. 19, pp. 924–933, Jun. 2002, doi: 10.1175/1520-0426(2002)019<0924:AESPAS>2.0.CO;2.

[21] H. B. Bluestein, M. M. French, I. PopStefanija, R. T. Bluth, and J. B. Knorr, "A mobile, phased-array Doppler radar for the study of severe convective storms: THE MWR-05XP," *Bull. Amer. Meteorolog. Soc.*, vol. 91, no. 5, pp. 579–600, May 2010, doi: 10.1175/2009BAMS2914.1.

[22] C. A. Balanis, *Modern Antenna Handbook*. Hoboken, NJ, USA: Wiley, 2011.

[23] I. R. Ivic, "Phase code to mitigate the copolar correlation coefficient bias in PPAR weather radar," *IEEE Trans. Geosci. Remote Sens.*, vol. 55, no. 4, pp. 2144–2166, Apr. 2017, doi: 10.1109/TGRS.2016.2637720.

[24] D. Zrnić, R. Doviak, G. Zhang, and A. Ryzhkov, "Bias in differential reflectivity due to cross coupling through the radiation patterns of polarimetric weather radars," *J. Atmos. Ocean. Technol.*, vol. 27, no. 10, pp. 1624–1637, Oct. 2010, doi: 10.1175/2010JTECHA1350.1.

[25] R. J. Doviak, V. Bringi, A. Ryzhkov, A. Zahrai, and D. Zrnić, "Considerations for polarimetric upgrades to operational WSR-88D radars," *J. Atmos. Ocean. Technol.*, vol. 17, no. 3, pp. 257–278, 2000, doi: 10.1175/1520-0426(2000)017<0257:CFPUTO>2.0.CO;2.

[26] M. Galletti and D. S. Zrnic, "Bias in copolar correlation coefficient caused by antenna radiation patterns," *IEEE Trans. Geosci. Remote Sens.*, vol. 49, no. 6, pp. 2274–2280, Jun. 2011, doi: 10.1109/TGRS.2010.2095019.

[27] B. Isom *et al.*, "The atmospheric imaging radar: Simultaneous volumetric observations using a phased array weather radar," *J. Atmos. Ocean. Technol.*, vol. 30, no. 4, pp. 655–675, Apr. 2013, doi: 10.1175/JTECH-D-12-00063.1.

[28] R. C. Hansen, *Phased Array Antennas*, vol. 213. Hoboken, NJ, USA: Wiley, 2009.

[29] C. J. Miller, "Minimizing the effects of phase quantization errors in an electronically scanned array," in *Proc. Symp. Electronically Scanned Phased Arrays Appl.*, 1964, pp. 17–38.

[30] K. Carver, W. Cooper, and W. Stutzman, "Beam-pointing errors of planar-phased arrays," *IEEE Trans. Antennas Propag.*, vol. AP-21, no. 2, pp. 199–202, Mar. 1973, doi: 10.1109/TAP.1973.1140434.

[31] M. I. Skolnik, *Radar Handbook*. New York, NY, USA: McGraw-Hill, 2008.

[32] M. D. Conway, D. D. Russel, A. Morris, and C. Parry, "Multifunction phased array radar advanced technology demonstrator nearfield test results," in *Proc. IEEE Radar Conf. (RadarConf)*, Apr. 2018, p. 1412, doi: 10.1109/RADAR.2018.8378771.

[33] I. R. Ivić, "An approach to simulate the effects of antenna patterns on polarimetric variable estimates," *J. Atmos. Ocean. Technol.*, vol. 34, no. 9, pp. 1907–1934, Sep. 2017, doi: 10.1175/JTECH-D-17-0015.1.

[34] I. R. Ivić, "Options for polarimetrie variable measurements on the MPAR advanced technology demonstrator," in *Proc. IEEE Radar Conf. (RadarConf)*, Apr. 2018, pp. 0129–0134, doi: 10.1109/RADAR.2018.8378544.

[35] I. R. Ivic, "Effects of phase coding on Doppler spectra in PPAR weather radar," *IEEE Trans. Geosci. Remote Sens.*, vol. 56, no. 4, pp. 2043–2065, Apr. 2018, doi: 10.1109/TGRS.2017.2772962.

[36] I. Ivic *et al.*, "An overview of weather calibration for the advanced technology demonstrator," in *Proc. IEEE Int. Symp. Phased Array Syst. Technol. (PAST)*, Oct. 2019, pp. 1–7, doi: 10.1109/PAST43306.2019.9021053.

[37] I. R. Ivić and D. Schvartzman, "A first look at the ATD data corrections. Preprints," in *Proc. 39th Int. Conf. Radar Meteorolog.*, 2019, pp. 1–8. [Online]. Available: https://cscenter.co.jp/icrm2019/program/data/abstracts/Poster2-06_2.pdf

[38] I. R. Ivić and D. Schvartzman, "Weather calibration efforts on the advanced technology demonstrator," in *Proc. 100th Amer. Meteorolog. Soc. Annu. Meeting*, 2020, pp. 2–8. [Online]. Available: https://ams.confex.com/ams/2020Annual/mediafile/Manuscript/Paper363084/ATD%20Calibration%20%28AMS%20Annual%202020%29%20Extended%20Abstract.pdf

[39] S. Torres *et al.*, "Towards an operational demonstration of the first full-scale polarimetric phased-array radar," in *Proc. 39th Int. Conf. Radar Meteorol.*, 2019.

[40] D. Schvartzman and S. M. Torres, "Distributed beams: A technique to reduce the scan time of an active rotating phased array radar system," in *Proc. 100th Amer. Meteorolog. Soc. Annu. Meeting*, 2020, pp. 1–10. [Online]. Available: https://ams.confex.com/ams/2020Annual/webprogram/Manuscript/Paper365842/Distributed%20Beams%20-%20Extended%20Abstract.pdf

[41] D. Schvartzman, S. M. Torres, and T.-Y. Yu, "Distributed beams: Concept of operations for polarimetric rotating phased array radar," *IEEE Trans. Geosci. Remote Sens.*, early access, Jan. 8, 2021, doi: 10.1109/TGRS.2020.3047090.

David Schvartzman (Member, IEEE) received the B.S. degree (*Summa Cum Laude*) in electrical and computer engineering from the National University of Asunción, Asunción, Paraguay, in 2011, and the M.S. and Ph.D. degrees in electrical and computer engineering from the University of Oklahoma, Norman, OK, USA, in 2015 and 2020, respectively. He is a Research Scientist with the Cooperative Institute for Mesoscale Meteorological Studies, The University of Oklahoma, which is affiliated with the National Severe Storms Laboratory. As a member of the Advanced Radar Techniques Team, he develops evolutionary signal processing algorithms to improve quality, accuracy, and timeliness of phased array radars. He also works on calibration and integration of phased array radar systems and supports the development of algorithms for the operational U.S. WSR-88D network.

Dr. Schvartzman is an Adjunct Instructor with the University of Oklahoma School of Electrical and Computer Engineering, where he teaches the Circuits Laboratory course. He is a graduate of the American Meteorological Society's (AMS) Early Career Leadership Academy (ECLA) and the recipient of the 2019 American Meteorological Society's Spiros G. Geotis Student Prize, for his article titled Design of Practical Pulse Compression Waveforms for Polarimetric Phased Array Radar.

Sebastián M. Torres (Senior Member, IEEE) received the B.S. degree from the National University of Mar del Plata, Mar del Plata, Argentina, in 1995, and the M.S. and Ph.D. degrees in electrical engineering from The University of Oklahoma, Norman, OK, USA, in 1997 and 2001, respectively.

In 1997, he joined the Cooperative Institute for Mesoscale Meteorological Studies at the University of Oklahoma, where he is the Assistant Director and a Senior Research Scientist with the National Severe Storms Laboratory (NSSL). He is also the Leader of the Advanced Radar Techniques Group at NSSL, conducting research and development of innovative signal processing and adaptive sensing techniques to improve the quality, coverage, accuracy, and timeliness of meteorological products from weather radars. He holds an Adjunct Faculty position with the School of Electrical and Computer Engineering, and is a member of the Graduate Faculty and the Advanced Radar Research Center, at The University of Oklahoma. He is involved in the exploration and demonstration of unique capabilities offered by phased-array radar for weather observations, and the transfer of technology to existing radar systems in government, public, and private organizations.

Dr. Torres received the 2011 Department of Commence Gold Medal as a member of the Radar Research and Development Division at NSSL for scientific and engineering excellence in adapting military phased-array-radar technology to improve U.S. weather radar capabilities, and the 2003–2004 Office of Oceanic and Atmospheric Research Outstanding Scientific Paper Award.

Tian-You Yu (Member, IEEE) received the Ph.D. degree in electrical engineering from the University of Nebraska, Lincoln, Nebraska, in 2000.

He then worked at the National Center for Atmospheric Research (NCAR) as a Post-Doctoral Fellow for two years before he joined the University of Oklahoma (OU), Norman, OK, USA, in 2002. This experience has provided him a unique cross-disciplinary background of atmospheric research using various sensors. His expertise includes the development and design of novel and sophisticated radar techniques with the goals of improving radar measurement, enhancing the warning of severe and hazardous weather, and advancing the fundamental knowledge of meteorological phenomena. In parallel with his technical strength, he has a passion for delivering high-quality education. He has developed and taught several undergraduate and graduate courses in the field of radar technology and science at OU. He is the Presidential Professor with the School of Electrical and Computer Engineering and an Adjunct Professor with the School of Meteorology, OU. He also serves as the Directors of Operations at the Advanced Radar Research Center (ARRC), which is an interdisciplinary research center.